Winter 2021

Efficient Modeling of an Array Antenna and Requirements for Maritime Mobile Reception of Meteorological Satellite Imagery

Alasdair Dunlap-Smith
University of New Hampshire

EFFICIENT MODELING OF AN ARRAY ANTENNA AND REQUIREMENTS FOR MARITIME MOBILE RECEPTION OF METEOROLOGICAL SATELLITE IMAGERY

BY

ALASDAIR DUNLAP-SMITH

BSc, Chemistry, Mount Allison University, 2010

THESIS

Submitted to the University of New Hampshire
in Partial Fulfillment of
the Requirements for the Degree of

Master of Science

in

Electrical and Computer Engineering

December 2021

This thesis has been examined and approved in partial fulfillment of the requirements for the degree of Master of Science in Electrical and Computer Engineering by:

Thesis Director, Dr. Michael J. Carter,
Associate Professor *emeritus* of
Electrical and Computer Engineering

Dr. Kent A. Chamberlin,
Professor *emeritus* of
Electrical and Computer Engineering

Dr. Nicholas J. Kirsch,
Professor of
Electrical and Computer Engineering

on December 2nd, 2021.

Original approval signatures are on file with the University of New Hampshire Graduate School.

TABLE OF CONTENTS

NOMENCLATURE

Roman Symbols

AF	Array factor
B	Bandwidth
D	Directivity
G	Gain
NF	Noise figure
S	Scattering coefficient
T_e	Equivalent noise temperature

Greek Symbols

Δ	Inter-element spacing
Γ	Reflection coefficient
θ	Beam forming angle from broadside
ε_r	Dielectric constant or relative permittivity
φ	Inter-element phase shift

Acronyms and Initialisms

APT	Automatic Picture Transmission
CGMS	Coordination Group for Meteorological Satellites
CSRR	Complementary Split-Ring Resonator
EUMETSAT	European Organization for the Exploitation of Meteorological Satellites
FDFD	Finite-Difference Frequency-Domain
FDTD	Finite-Difference Time-Domain
GMDSS	Global Maritime Distress and Safety System

GOES	Geostationary Operational Environmental Satellite
GRB	GOES-R Re-Broadcast
HRIT	High-Rate Information Transmission
HRPT	High-Resolution Picture Transmission (Advanced-, Color-)
ITU	International Telecommunication Union
JPSS	Joint Polar Satellite System
LRPT	Low-Rate Picture Transmission
MetOp	Meteorological Operational Satellite
NAVTEX	Navigational Telex
NOAA	National Oceanic and Atmospheric Administration
NPOESS	National Polar-orbiting Operational Environmental Satellite System
OSCAR	Observing Systems Capability Analysis and Review
PID	Proportional-Integral-Derivative
POES	Polar Operational Environmental Satellite
SMA	Sub-Miniature A
VNA	Vector Network Analyzer
WMO	World Meteorological Organization

LIST OF TABLES

Table **Page**

LIST OF FIGURES

Figure **Page**

ABSTRACT

Efficient modeling of an array antenna and requirements for maritime mobile reception of meteorological satellite imagery

by

Alasdair Dunlap-Smith

University of New Hampshire, December, 2021

Wireless communication is an integral part of safety at sea. Direct broadcasts from public weather satellites on L- and X-band provide real-time weather observations and weather product dissemination to end users. These high-bandwidth broadcasts offer enhanced data throughput and require accurate pointing of high-gain antennas.

An electronically-steered array antenna can provide high gain and rapid beam steering without moving parts, suitable for deployment on small vessels offshore. Figures of merit, such as array antenna gain and input impedance, vary with the beam steering angle as a consequence of mutual coupling between array elements. The electromagnetic design of an electronically-steered array antenna is more complex than a parabolic dish or a fixed broadside array, requiring an iterative development process and a computationally efficient method of simulating the array.

This work addresses the validation of an efficient method for array simulation, a necessary first step in the design process of a deployable array. Starting with a small L-band subarray, a Fourier windowing method is applied to approximate the scan-dependent behavior of an electronically-steered array from an efficient numerical model in a periodic unit cell. Results are validated against experimental measurements of hardware prototypes and explicit numerical models of the subarray. The iterative design of antenna elements in an array environment and construction of a full-size array are left for future work.

CHAPTER 1

INTRODUCTION

Satellites bring high-bandwidth wireless communication to the open ocean. Direct broadcasts from public weather satellites provide real-time weather observations and weather product dissemination to end users, but current-generation satellites have deprecated high-power VHF broadcasts in favor of downlinks exclusively on L- and X-band. The new high-bandwidth broadcasts offer enhanced data products and require accurate pointing of high-gain antennas.

An electronically-steered array antenna can provide high gain and rapid beam steering without moving parts, suitable for deployment on small vessels subject to large accelerations and beam slew rates. Figures of merit, such as array antenna gain and input impedance, vary with the beam steering angle as a consequence of mutual coupling between array elements. The electromagnetic design of an electronically-steered array antenna is more complex than a parabolic dish or fixed broadside array, requiring an iterative development process and a computationally efficient method of simulating the array.

1.1 Contribution of this work

This work identifies a combination of bounded design space and numerical approximation with sufficient efficiency and accuracy to support an iterative design process for a full-size array. As such, this work concerns validation of a workflow, the preliminary stage of the design process for a deployable array antenna. The iterative design of antenna elements in an array environment and construction of a full-size array for a particular application are left for future work.

For a uniform array antenna with sufficient size and gain to receive weather satellite broadcasts, numerical simulation with an explicit whole-array model is not computationally efficient because many of the elements in the array interior experience the same coupling environment. Simulation

with a periodic unit cell, where the array is approximated as infinitely large, is not physically efficient as the finite array must be enlarged to compensate for elements detuned by edge effects.

Starting with a small L-band subarray, a Fourier windowing method developed for fixed broadside arrays is used to approximate the scan-dependent behavior of an electronically-steered array from a numerically efficient model in a periodic unit cell. Results are validated against experimental measurements and explicit numerical models of the subarray. The optimal design for an element embedded in an array depends on the relative number of edge elements in the array, a function of the array size as described in Section 2.3. With the method validated in this work, antenna elements can be optimized for performance while embedded in an array of any finite size.

1.2 Maritime mobile radio communication

The Global Maritime Distress and Safety System (GMDSS) is a set of international standards for maritime communication jointly maintained by the International Maritime Organization (IMO) and the International Telecommunication Union (ITU). Commercial shipping and other large vessels are required to carry multiple wireless communication systems depending on their geographic area of operation including MF, HF, and VHF terrestrial voice/data and satellite terminals. Recreational sailors on small vessels offshore are exempt from many GMDSS requirements but still benefit from data broadcast services such as MF NAVTEX that can be received with compact and inexpensive equipment.

Ongoing efforts to modernize GMDSS standards reflect an overall shift from terrestrial analog and low-bandwidth digital modes to high-bandwidth satellite services [6]. Most large vessels already have access to high-bandwidth satellite services such as Inmarsat and Iridium and in the United States, MF broadcasts of NAVTEX data may soon be discontinued entirely in favor of satellite dissemination [7]. The size and cost of a mechanically-stabilized dish antenna is prohibitive for many recreational sailors, and the active motion of a small vessel often exceeds the specifications of commercial motorized gimbals.

(a) Approaching cloud mass.

(b) Funnel cloud.

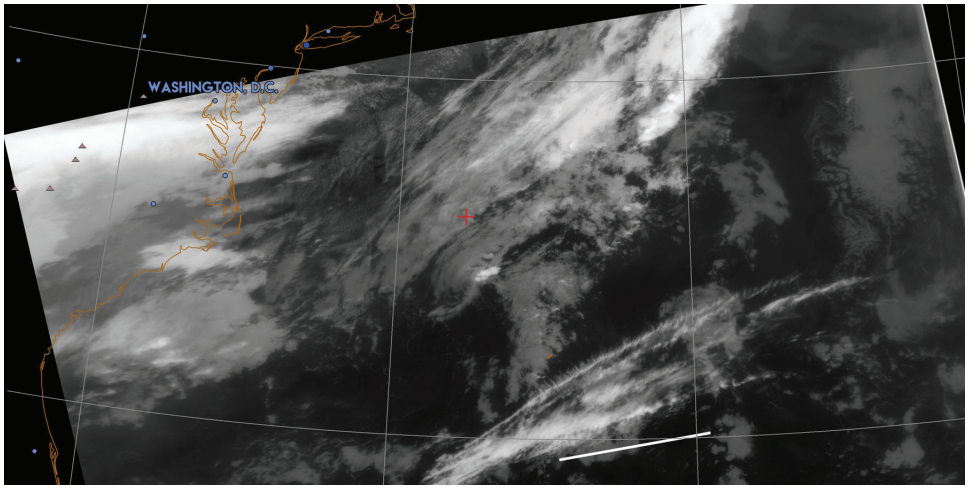

(c) Satellite image of the frontal boundary (10.5-11.5 μm IR, Meteor-M N2). UTM projection with 10° lat/lon grid, vessel position marked +.

Figure 1.1: Maritime mobile reception of direct broadcast satellite imagery providing context for locally observable weather.

For recreational sailors on small vessels offshore, data needs are met by managed text-messaging services with hand-held satellite communicators and low-gain antennas (Globalstar, Iridium short burst data), voice and low-rate data over single-sideband HF/MF radio, and reception of direct broadcast imagery from polar-orbiting weather satellites.

Timely access to satellite imagery, as provided by direct broadcast services, is especially valuable to small sailing vessels that must make efficient use of favorable weather while avoiding hazards. Crew decisions to proactively alter course and trim for vessel speed or safety margin are often timed around the expected arrival of synoptic-scale weather features such as frontal boundaries. The correct identification of an approaching weather feature is not always unambiguous from local observables: in Figure 1.1a, an overtaking cloud mass could be an expected cold front, or another prefrontal disturbance. Multiple funnel cloud sightings, as in Figure 1.1b, indicated an additional wind hazard, and weather satellite imagery in Figure 1.1c confirmed that the leading edge of a frontal boundary had arrived.

1.3 Direct-broadcast services

Many earth-observing weather satellites broadcast multispectral imagery and derived weather products directly to end users in the field. Parallel to the modernization of GMDSS, weather satellite direct broadcast services are also adopting steered high-gain ground station antennas as a minimum requirement for user terminals.

Satellite weather observation broadcasts on VHF are nominally available to small vessels from three constellations: POES (NOAA, United States), MetOp (EUMETSAT, European Union), and Meteor-M (Roshydromet, Russia). The POES series is deprecated; of the final five satellites with a five-year planned lifetime, three are fully or partially operational after 12 to 23 years in orbit.[1] POES satellites continue to broadcast two-channel visible and IR images with 4km/pixel resolution via an analog modulation scheme, Analog Picture Transmission (APT).

[1]The final satellite in the POES-5 series, NOAA-19, is relatively young with a 2009 launch date, following an extensive rebuild after the satellite fell off a cart during testing in 2003 [8].

VHF APT broadcasts occupy 38 kHz-wide slots in the 137-138 MHz satellite band and can be received with a FM radio and computer sound card [9]. The convergence of falling hardware costs and increasing computational performance now favors demodulation and decoding in software with minimal RF hardware (software-defined radio) [10]. Re-purposed consumer USB sticks for digital television reception using the Realtek RTL2832U integrated circuit[2] provide a complete software-defined radio receiver with 2.5 MHz bandwidth for around $20 [12]. The example APT image in Figure 1.2 was captured with a dipole antenna and a RTL2832U-based receiver.

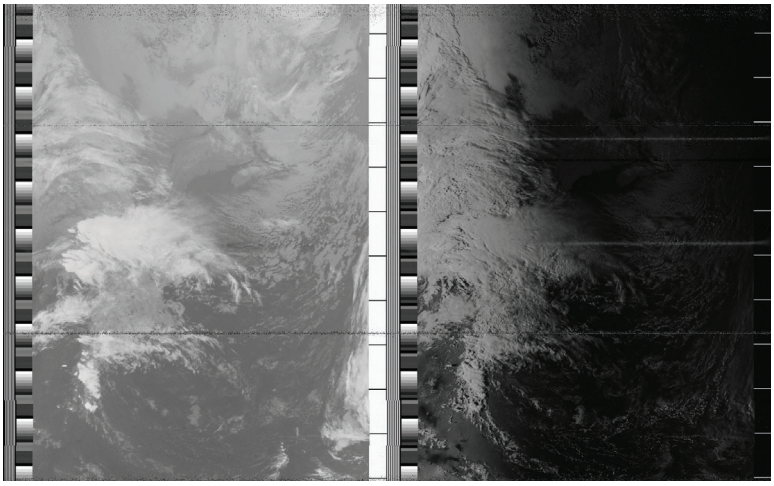

Figure 1.2: POES APT two-channel VHF direct broadcast.

Following the POES-5 series of satellites, Low-Rate Picture Transmission (LRPT), a digital modulation for VHF broadcasts developed by EUMETSAT to replace APT, was adopted as part of an effort to share instrumentation and polar orbit slots between the next-generation of NOAA satellites, NPOESS, and the first generation of ESA polar-orbiting satellites, MetOp [13]. LRPT supports compressed three-channel images with up to 1km/pixel resolution at the track center via a 72 kBaud QPSK digital modulation operating with 150 kHz bandwidth on the same 137 MHz carrier frequency as APT [14].

[2]Via an undocumented feature bypassing the on-chip DVB-T hardware decoder to access raw I/Q samples over USB [11].

The NPOESS design was ultimately cancelled after 16 years. The LRPT transponder on the first MetOp satellite was disabled after launch when it interfered with the radiometer [1] and the LRPT service was abandoned on subsequent MetOp launches. No subsequent NOAA or EUMETSAT satellites have implemented a VHF direct broadcast service. LRPT broadcasts on VHF are available from Roshydromet/Roskosmos' Meteor-M series of polar-orbiting satellites. One Meteor-M satellite is currently operational, with another launch planned before 2022. The example image in Figure 1.3 was received using the same low-cost receiver and dipole antenna as in Figure 1.2.

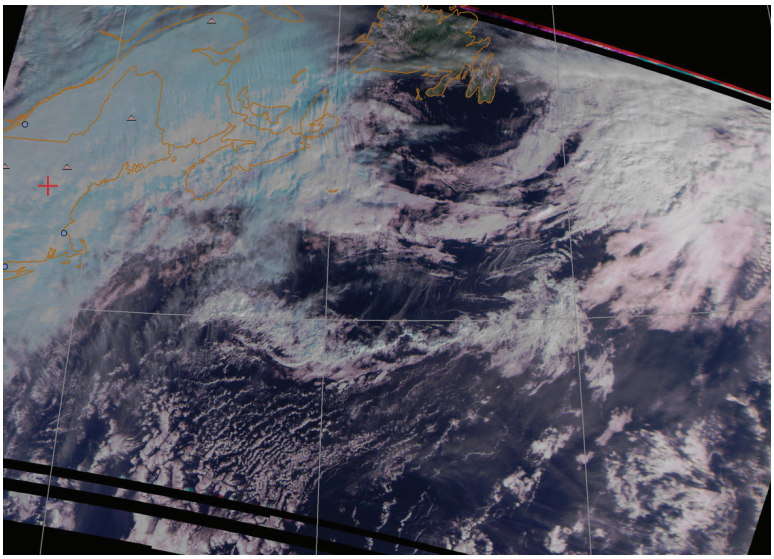

Figure 1.3: Meteor-M N2 LRPT three-channel VHF direct broadcast.

Primary direct broadcast services from current-generation weather satellites are on L-band at 1.7 GHz. Next-generation polar-orbiting weather satellites such as JPSS and MetOp-SG will broadcast exclusively on the meteorological X-band at 7.8 GHz. A summary of direct broadcast services from current and future weather satellite systems is provided in Table 1.1.

At the request of the Coordination Group for Meteorological Satellites (CGMS) and the World Meteorological Organization (WMO), the ITU allocated the 1675-1710 MHz band in Region 2 on a primary basis for existing and future meteorological satellites following the 1992 World Administrative Radio Conference (WARC-92). This allocation was divided into three sub-bands:

Series	Availability	Service	Band
POES 5th gen.	1998 – Present	APT	VHF
POES 5th gen.	1998 – Present	HRPT	L-band
MetOp	2006 – 2007	LRPT	VHF
MetOp	2006 – Present	AHRPT	L-band
MetOp-SG	2024	HRD	X-band
S-NPP/JPSS-1	2011 – Present	HRD	X-band
JPSS-2+	2022	HRD	X-band
JPSS-2+	~~2022~~ *Cancelled*	~~LRD~~	L-band
Meteor-M N2	2014 – Present	LRPT	VHF
Meteor-M N2	2014 – Present	MHRPT	L-band
FengYun-3	2008 – Present	CHRPT	L-band
FengYun-3	2008 – Present	MPT	X-band
GOES-R	2016 – Present	HRIT	L-band
GOES-R	2016 – Present	GRB	L-band

Table 1.1: Direct broadcast services available from current and future weather satellite systems. All satellites occupy sun-synchronous polar orbits except the geostationary GOES-R series (United States), which is representative of other national geostationary observatories not listed. Data from the WMO OSCAR service [1].

1675-1690 MHz for raw data collection from geostationary satellites,[3] 1690-1698 MHz for direct broadcasts from geostationary satellites, and 1698-1710 MHz for direct broadcast from sun-synchronous polar-orbiting satellites and other non-geostationary systems [15]. Meteorological users represented by the CGMS are competing for spectrum with various commercial interests; in the first decade after WARC-92, all attempts to expand protections for meteorological services failed and an increasing number of commercial services attempted to gain access to the existing region 2 allocation [16].

In the last decade, commercial interests in the United States have made inroads into the meteorological L-band allocation. Following an act of Congress in 2012, the NTIA was directed to find 15 MHz of spectrum within the 1675-1710 MHz band to auction to commercial mobile broadband providers. The NTIA recommended the 1695-1710 MHz segment to the FCC for reallocation [17]

[3]GOES-R Re-Broadcast (GRB), a high-resolution direct broadcast service, now occupies 11.6 MHz of bandwidth with a 1686.6 MHz carrier. The raw data link for GOES-R-series satellites is on X-band at 8220 MHz [2]

and the spectrum was sold as part of the AWS-3 auction in 2015; the 1695-1710 MHz segment is now allocated for LTE band 70 uplinks as part of a new 5G network build-out by DISH Wireless.

Although the FCC prioritized clearing existing users before auctioning spectrum blocks, this was not feasible in the 1695-1710 MHz segment due to the incumbent satellite services, and protection zones of 20-100 km radius were established around 27 federally-operated earth stations.[4] Despite opposition from the WMO at the 2015 WRC [18] and vulnerability of both HRPT and adjacent-channel HRIT receiving stations to interference from LTE handsets [19, 20], users outside the 27 federal protection zones have no protection under current rules [21].

1.4 Alternatives to planar arrays

Any set of antenna elements can function as a beamforming array. The elements do not need to be identical or arranged in any organized fashion. Designing such an arbitrary array is non-trivial and requires costly simulations of the entire array. A more practical realization of a complex array might deploy a small set of element designs into different array zones to compensate for edge effects, or a uniform array of identical elements conforming to a curved surface to maintain aperture efficiency at large scan angles.

In this work, the design space is restricted to uniform planar rectangular arrays: arrays of identical antenna elements, arranged on a planar rectangular grid. These restrictions reduce the number of adjustable parameters and simplify the synthesis of the array from the properties of individual elements embedded in an array environment.[5]

The uniform planar rectangular array motif simplifies analysis, but aperture efficiency is poor at large scan angles. This scan loss, the gain variation with scan angle θ from broadside resulting from reduced projected aperture, is proportional to $\cos\theta$. The input impedance of the planar array also varies with scan angle, introducing an additional scan-dependent loss. Gain variation proportional

[4] See 47 CFR 2.106 footnote US 88.

[5] Irregular arrays of identical elements located on a uniform lattice can reduce the number of elements required to achieve a required side lobe level or other figure of merit, without greatly increasing the design complexity. Clustered, thinned, and sparse arrays are examples of this design concept. [22]

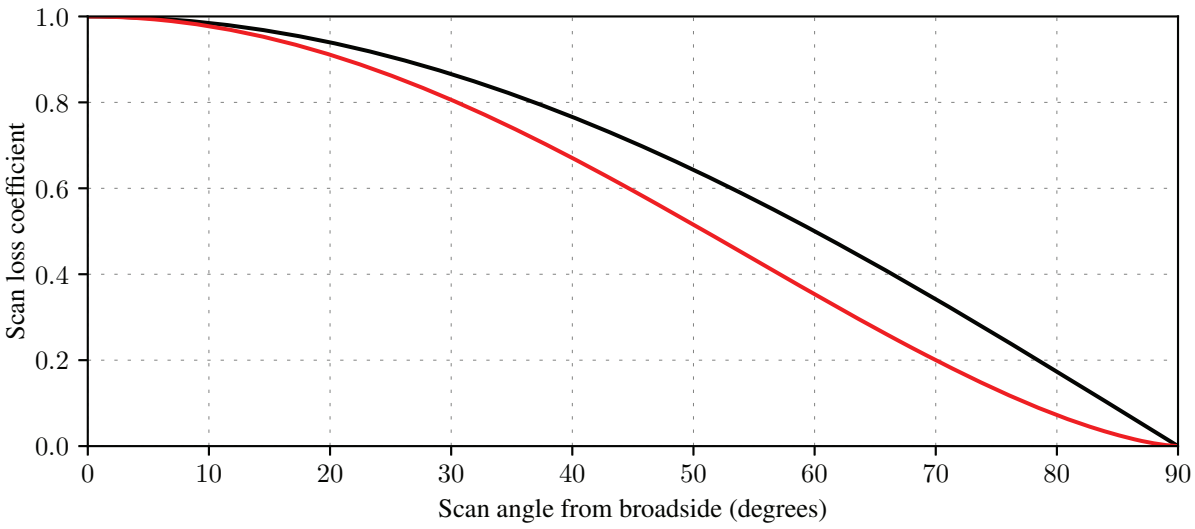

Figure 1.4: Scan loss of a planar array: ideal relation to projected aperture $\cos\theta$ — and empirical curve for a 2-D array including scan-dependent input impedance $\cos^{3/2}\theta$ —.

to $\cos^{3/2}\theta$ is a good empirical approximation combining both effects for a well-designed 2-D planar array [23, pp. 25-26]. Both the ideal scan loss resulting from projected aperture and the empirical scan loss are illustrated in Figure 1.4. Practical planar arrays are restricted to scan angles $\theta < 90°$.

The undesirable variation in array gain resulting from scan loss can be avoided by conforming the uniform array to a spherical surface with constant projected aperture. This has been implemented for maritime mobile Inmarsat satellite terminals as a uniform array conforming to a cylindrical surface with reduced scan loss in one axis [24], and as a set of planar subarrays assembled into faces of a polyhedron, an approximate sphere [25]. Both array designs exceed the maximum scan range of a planar array in one or two axes.

The small planar subarray examined in the following chapters serves to compare numerical methods with varying accuracy and efficiency. In a practical application, an optimized planar subarray can be scaled up to a full-size planar array achieving sufficient gain at the maximum desired scan angle, or assembled in a polyhedron of planar subarrays.

CHAPTER 2

ARRAY NETWORK THEORY

The infinite array approximation, realized in a periodic unit cell, is an acceptable compromise for large arrays that trades peripheral element performance in exchange for a very compact computational domain. In a large uniform array of identical elements, elements detuned by edge effects are poorly represented by the unit cell model but comprise only a small portion of the total number of array elements. Practical constraints on the physical size of an L-band array require that all array elements contribute to the array directivity and gain to achieve the required performance without the cost and space burden of passive or under-utilized edge elements.

In this work, all constructed prototype subarrays are linearly polarized with the E-plane in the $\vec{y}$ direction, the H-plane in the $\vec{x}$ direction, and the array broadside ($\theta = 0°$) in the $\vec{z}$ direction. This chapter briefly reviews aspects of network theory, as applied to a uniform array. For a review of antenna patterns and figures of merit, see the article by Balanis [26]. Microwave network analysis is summarized from Pozar [27].

2.1 Antennas and networks

The basic form of the antenna is a one-port network that couples a guided wave on a transmission line to a radiating wave in free space. Radiation intensity $U(\theta, \phi)$ is the radiated power P_r per unit solid angle in the direction θ, ϕ. Directivity $D(\theta, \phi) = U(\theta, \phi) \cdot {}^{4\pi}/_{P_r}$ is the radiation intensity U normalized by the radiation intensity of an isotropic antenna $U_0 = {}^{P_r}/_{4\pi}$, where 4π is the solid angle of a unit sphere. The directivity of an isotropic antenna is then $D_0 = 1 = 0$ dB; a perfect hemispherical radiator, such as an isotropic antenna on a ground plane, has directivity $D(\theta, \phi) =$ 3 dB for $0° \leq \theta \leq 90°$.

Allowing for dissipation in lossy materials, radiated power $P_r = e_r P_a$ will be less than the accepted power P_a by an efficiency factor $e_r \leq 1$, and antenna gain is then $G = e_r D$. The accepted power P_a will be less than the incident power P at the antenna port due to reflection from impedance mismatch, and the realized gain is

$$G_r = (1 - |\Gamma|^2)\, G \tag{2.1}$$

where $\Gamma = {}^{z-1}/_{z+1}$ is the voltage reflection coefficient and z is the port impedance $Z = {}^{V}/_{I}$ normalized to a reference impedance, typically $z_0 = 50\,\Omega$.

The scattering parameter $S = {}^{V^-}/_{V^+}$ is the complex ratio of the reverse or reflected voltage V^- to the forward or incident voltage V^+ on the transmission line at the antenna port. For ports $i, j \in N$ of an N-port network such as the antenna array in Figure 2.1, the matrix of scattering parameters $S_{ij} = {}^{V_i^-}/_{V_j^+}$ assumes that there is no forward voltage $V_k^+ = 0$ on all other ports $k \neq j$, where ports k are terminated with perfectly matched loads [27]. For practical measurements with an instrument such as a 2-port vector network analyzer (VNA), the condition of zero reflected power is approximated with resistive terminators.

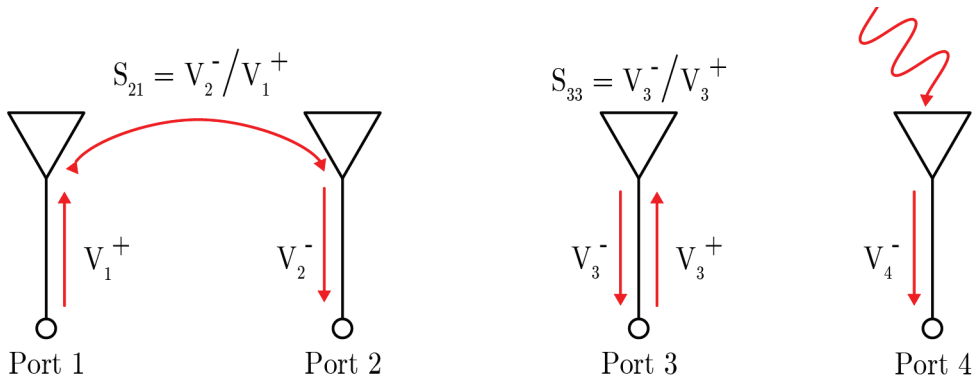

Figure 2.1: Orientation of array antenna port voltages and scattering parameters.

2.2 Active element pattern

Temporarily setting aside any coupling effects, the realized gain of a uniform 1D array is $G_{array} = G_r \cdot AF$ where G_r is the realized gain of a single antenna element in isolation and the array factor AF is the sum of per-element excitation weights and phase shifts:

$$AF = \sum_{n=0}^{N-1} A_n e^{jn\varphi} = \sum_{n=0}^{N-1} A_n e^{jn \cdot dk \sin(\theta)} \tag{2.2}$$

For a uniformly-illuminated array ($A_n = 1$ for all n) scanned to broadside ($\theta = 0°$), $AF = N$ and array gain $G_{array} = N \cdot G_r$. In this notation, φ is the phase shift between adjacent elements, d is the array element spacing in distance units, $k = {}^{2\pi}/_{\lambda}$ is the angular wavenumber, and θ is the beam steering angle measured from broadside.

In a real array, mutual coupling between elements is unavoidable[1] [28] and results in non-zero scattering parameters S_{ij} for $i \neq j$. The array gain cannot be described as the product of the array factor and isolated element gain pattern, but mutual coupling can be included in this formalism by replacing the isolated element pattern with an active element gain pattern G_{active},[2] defined as the radiation pattern obtained by exciting a single element in an array with all other elements match-terminated. Note that for a uniform array of identical elements, the active element pattern will vary depending on the local environment of a particular element: an element at the edge of the array experiences different mutual coupling than an element in the center of the array [30].

For model validation, the difficult task of measuring the gain pattern G_{array} for a fully-excited array at a variety of scan angles is then replaced by the measuring the active element patterns

[1] As a consequence of this inevitability, analysis of antenna elements in isolation has little value in array synthesis. The 2018 edition of R. J. Mailloux's reference text on antenna arrays discards most material on the impedance and gain properties of isolated antenna elements, prefaced with the explanation that "the characteristics of an isolated antenna element have little to do with the pattern of the same element in an array." [23].

[2] The description of so-called active elements has been described as "obsolete and misleading" [29] but "active" elements and "active" impedances are still common in the literature and is used here. The term "scan element pattern" is sometimes substituted.

G_{active} for a representative selection of array elements. Measuring a set of far-field patterns is still non-trivial, but this can be replaced by measuring only the terms of the array scattering matrix S_{ij}.

The active reflection coefficient $S_{ii_{\text{active}}}$ for element i in the array is the reflection coefficient for one element in a fully-excited array, obtained as the complex ratio of the reflected voltage V^- and incident voltage V_i^+, where V^- includes the voltage coupled from other elements $V^- = S_{ij}V_j^+$:

$$S_{ii_{\text{active}}}^{(\varphi)} = \frac{\sum_j S_{ij}V_j^+}{V_i^+} \tag{2.3}$$

The forward voltage on array element n has a complex phase $e^{jn\varphi} = e^{jn \cdot dk \sin(\theta)}$ following the array factor and the active reflection coefficient depends on the scan angle. Mutual coupling must be mitigated to reduce scan-dispersion of the active reflection coefficient.

The array gain pattern with the array scanned to beam angle θ is then obtained from the active reflection coefficient as in Equation (2.1):

$$G_{array} = \sum G_{active} = \sum G_r \left(1 - |S_{ii_{\text{active}}}^{(\varphi)}|^2\right) = G_r \sum \left(1 - |S_{ii_{\text{active}}}^{(\varphi)}|^2\right) \tag{2.4}$$

where G_r is the realized gain of a single antenna element in isolation. The active element gain pattern is then directly related to the active reflection coefficient [31] and this relationship can be inverted [32]. The matrix of complex scattering coefficients S_{ij}, the scattering matrix, provides a complete description of the array with mutual coupling at an arbitrary scan angle.

2.3 Finite array scattering matrix

The scattering matrix for a finite array can be measured directly with a VNA or modeled with an electromagnetic solver. As mutual coupling in a uniform planar array is dominated by short-range interactions between adjacent elements, measurements of reduced-size subarrays are a useful design tool when the element geometry is complex or computationally expensive. For very large arrays, the majority of array elements are not near the array edges and experience approximately the same coupling environment. Under this condition an infinite array of elements with identical active reflection coefficients is a good approximation, and can be implemented in models as a unit

cell with periodic linked boundaries [23, pp. 315-319]. The minimum size for a subarray that contains central elements approximately insulated from edge effects is empirically estimated at $5\lambda \times 5\lambda$, corresponding to a 10×10 element subarray with narrow bandwidth and 0.5λ element spacing [33]. Of the 100 elements in the 10×10 subarray, the central four elements approximate an infinite array environment and the remaining 96 elements constitute a four-element wide buffer perturbed by edge effects.

A suitable L-band array that meets the design goals of this work will require a 2-D array on the order of 200 elements:[3] too large for iterative design with full-size prototypes or explicit computational models, but too small to entirely neglect edge effects with a computationally efficient periodic unit cell.

Several methods have been developed to reconstruct properties of a finite array from infinite array data using Fourier windowing techniques. These methods assume an excited subarray embedded in an infinite array, where coupling between two elements depends only on the distance between the elements independent of the position within the excited subarray [35].

This assumption is valid for minimum scattering elements, a condition fulfilled exactly when reconstructing the finite admittance matrix Y of a slot or waveguide array (shorted waveguides become an infinite ground plane[4]) or the finite impedance matrix $Z = Y^{-1}$ of a dipole array (open-circuited dipoles are good approximations of minimum scatterers).

The technique validated in this work reconstructs the finite scattering matrix from the active reflection coefficient of an element in an infinite array: Starting from a single-element (1-port) unit

---

[3]As an estimate of array size for a target gain of 24 dBi sufficient for weather satellite broadcasts [9, p. 66], an array of elements with 2 dBi gain requires an additional 22 dB of array gain. As the array gain is proportional to the number of elements [34], this suggests an array with at least 159 elements (such as a 13×13 array of 169 elements) at broadside scan $\theta = 0°$, or a minimum of 316 elements (such as an 18×18 array of 324 elements) if the array is scanned to $\theta = 50°$ assuming 3 dB of scan loss following Figure 1.4. Allowing a four-element wide buffer of elements perturbed by edge effects [33], only the central 100 elements in an 18×18 array of 324 elements approximate the infinite array environment assumed by a periodic unit cell. Inside the meteorological L-band segment, at $f = 1700$ MHz, $\lambda = 176.4$ mm, an 18×18 element array with typical 0.5λ element spacing will have a nominal edge length of $9\lambda = 1.59$ m, comparable to a standard 60-cell photovoltaic panel (1.02×1.68 m) commonly deployed on small vessels in fixed and temporary mountings. The addition of a four-element wide annular buffer zone would expand the array to 26×26 with 576 elements, measuring 2.29 m on a side.

[4]Neglecting the effect of a finite ground plane on edge elements in a practical array.

cell model for a 2D array in the x, y plane, the active reflection coefficient $S_{11_{\text{active}}}^{(\varphi_x,\varphi_y)}$ can be evaluated for over the range of phase shifts φ_x, φ_y by introducing a corresponding phase shift at the unit cell boundaries. The complex scattering coefficient S_{ij} between elements i and j in a finite array can then be approximated with Eq. (2.5), a Fourier integral in phase-space. $(\vec{s}_j - \vec{s}_i)$ is the coordinate vector between array elements (network ports) i and j, normalized by the element spacing $\Delta_{x,y}$, and $\vec{u}_{x,y}$ is the pair of corresponding unit vectors.

$$S_{ij} = \frac{1}{4\pi^2} \int_0^{2\pi} \int_0^{2\pi} S_{11_{\text{active}}}^{(\varphi_x,\varphi_y)} e^{-j(\varphi_x \vec{u}_x + \varphi_y \vec{u}_y)\cdot(\vec{s}_j - \vec{s}_i)} \cdot \delta\varphi_x \cdot \delta\varphi_y \tag{2.5}$$

This "reconstruction" of the finite array scattering matrix from the periodic unit cell still assumes an infinite array; a finite subarray is excited and all other elements are match-terminated. This approximation of a finite array is accurate for waveguide arrays and acceptable for patch arrays [36, 37]. Experimental validation with a design for a fixed broadside 64×16 element patch array demonstrated favorable performance [38]. For practical applications, the array design should have good isolation between the radiating elements and the feed network so that the feed network can be modeled separately from the unit cell.

Although the reconstructed scattering matrix is not used in this work to design the initial subarrays in Chapter 3, it is validated against measurements and explicit models in preparation for efficient modeling of the full-size array.

CHAPTER 3

DESIGN OF AN L-BAND ARRAY

In this chapter, an array of resonant patch elements with aperture feeds is designed starting from transmission line theory.

The properties of the patch element are well-matched to an L-band array for weather satellite broadcast reception: wide bandwidth is not required, and the small electrical size of the patch allows for a 0.5λ element spacing.[1] The choice of a patch element for this work does not preclude other element designs: folded dipole arrays, either printed on flat panels or assembled for edge launch in an 'egg crate' structure,[2] are practical alternatives to patch elements for arrays with large scan angles.

The design of a deployable array necessarily follows an integrated process. Electromagnetic, mechanical, and environmental requirements impose inseparable constraints on the array geometry. The initial prototypes developed in this work do not need to endure exposure to the elements, but considering these constraints provides some initial design guidance before the use of integrated models.

Starting with Section 3.1, the need for a stiff, lightweight, and weatherproof structure suggests an array printed on stacks of planar sheets. Section 3.2 identifies a suitable array element, and a method of feeding the array elements from an isolated feed network compatible with the mechanical structure outlined in Section 3.1. After numerical optimization of the element geometry in Section 3.3, small subarrays are modeled in Section 3.4. Finally, Section 3.5 augments a simple two-element subarray with an auxiliary structure to mitigate mutual coupling.

---

[1] An element spacing of approximately 0.5λ is typical in uniform arrays. This suppresses spurious array pattern lobes in real space. The element spacing may be increased if the array is designed for a restricted scan range [23].

[2] Also known as the brick and tile architectures for assembly of arrays from PCBs [23].

3.1 Mechanical properties of the array

Although the electronically-steered array antenna has no moving parts, other desirable mechanical properties inform aspects of the element design: the array should be lightweight to easily stow and deploy, stiff to maintain the planar geometry subject to forces from wind and vessel motion, and impervious to salt spray and prolonged sun exposure. An array of patch elements constructed as a sandwich structure achieves all of these properties with minimal cost and complexity.

A flat panel with unit width has a flexural rigidity D proportional to the flexural modulus E of the panel and the cube of the panel thickness h:

$$D = \frac{h^3 E}{12} \tag{3.1}$$

For a balanced sandwich panel with core thickness h_c, skin thickness h_s, and total thickness $h = h_c + 2h_s$, the effective flexural modulus E_f is:

$$E_f = E_c v^3 + E_s(1 - v^3) \tag{3.2}$$

where $v = h_c/h$ is the ratio of the core thickness to the total panel thickness [39].

Sandwich structures with high-modulus skins bonded to a low-density core offer high flexural rigidity per weight. For example, consider the flexural rigidity of three panels: *a*) FR4 epoxy/glass composite with thickness $h_s = 3.2$ mm, *b*) Rohacell 51 HF dielectric foam with thickness $h_c = 19$ mm, and *c*) a sandwich structure with two FR4 skins, each with thickness $h_s = 1.6$ mm, and a Rohacell core with thickness $h_c = 19$ mm. The effective flexural modulus of the sandwich structure is $E_f = 9.0$ GPa per Equation (3.2). The flexural rigidities of the three panels are listed in Table 3.1.

The sandwich structure offers a ≈100x improvement in stiffness compared to a thin FR4 panel and can be easily assembled by vacuum bag laminating against a flat mold. Bonding the upper skin 'upside-down' with the patches contacting the foam spacer leaves the bare side of the FR4

	Panel thickness h	**Modulus** E	**Flexural rigidity** D
FR4	3.2 mm	24 GPa	66 Pa·m^4
Rohacell 51 HF	19 mm	70 MPa	40 Pa·m^4
FR4/Rohacell sandwich	22.2 mm	9.0 GPa	8200 Pa·m^4

Table 3.1: Flexural rigidity of uniform and sandwich panels.

skin exposed on top. This protects the antenna elements from corrosion and the FR4 surface can be finished with a cross-linked polyurethane or other conventional coating for sun exposure, obviating the need for a separate radome as in an egg-crate structure.

3.2 The patch element

A flat conductor suspended over a ground plane functions as a simple TEM transmission line. Filling the space between the conductor and ground plane with a dielectric substrate complicates the analysis of the transmission line, as the electric and magnetic fields are not fully contained in the dielectric layer. Provided that the substrate thickness h is thin compared to the width of the conductor W, the behavior of the transmission line is quasi-TEM [27, pp. 147-148] and approximated by a TEM transmission line suspended in a medium with an effective dielectric constant ε_{eff} given by Equation (3.3).

$$\varepsilon_{eff} = \frac{\varepsilon_r + 1}{2} + \frac{\varepsilon_r - 1}{2}\left(\frac{1}{\sqrt{1 + 12h/W}}\right) \tag{3.3}$$

This transmission line, the common microstrip, is used in this work to feed array elements. The characteristic impedance of the microstrip transmission line, for $W/h \geq 1$, is then:

$$Z_0 = \frac{120\pi}{\sqrt{\varepsilon_{eff}}} \times \frac{1}{W/h + 1.393 + 0.667\ln\left(W/h + 1.444\right)} \tag{3.4}$$

A $Z_0 = 50\Omega$ microstrip on a 1.6 mm-thick FR4 substrate with a dielectric constant $\varepsilon_r = 4.3$ has width $W = 3.1$ mm.

A rectangular patch antenna resonant at free-space wavelength λ_r, with length L and width W and suspended at height h above a ground plane, can be modeled approximately as a pair of radiating slot antennas with slot dimensions $W \times h$, connected by a $L = 0.5\lambda$ section of transmission line. As configured for linearly polarized radiation, the transmission line is oriented in the E-plane and the radiating slots are oriented in the H-plane. Equations (3.5) to (3.7) are an empirical prescription for a rectangular patch antenna based on this transmission line model, commonly used in reference texts [40, pp. 790-791]. The dimensions, planes, and coordinate axes used in this work are illustrated in Figure 3.1.

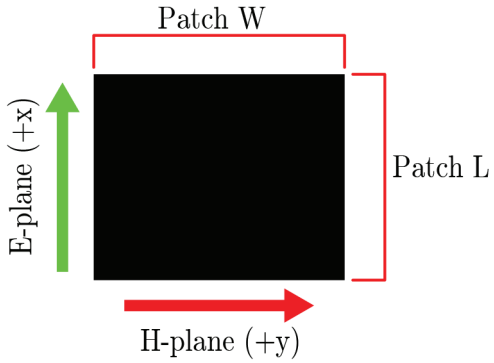

Figure 3.1: Dimensions and orientation of a linearly-polarized rectangular patch.

The physical length of a patch given by Equation (3.5) is half of a wavelength in the effective dielectric medium obtained from Equation (3.3). The correction factor ΔL is attributed to fringing fields at the ends of the patch that increase the effective length of the transmission line.

$$L = \frac{\lambda_r}{2\sqrt{\varepsilon_{eff}}} - 2\Delta L \tag{3.5}$$

$$\Delta L = 0.412h\frac{(\varepsilon_{eff} + 0.3)\left[\frac{W}{h} + 0.264\right]}{(\varepsilon_{eff} - 0.258)\left[\frac{W}{h} + 0.8\right]} \tag{3.6}$$

$$W = \frac{\lambda_r}{2}\sqrt{\frac{2}{\varepsilon_r + 1}} \tag{3.7}$$

A square patch can be dual-polarized with separate feeds; if the patch antenna only requires linear polarization, an empirical formula for the optimal width of the patch is given by Equation (3.7). Although this formula is widely reproduced, it was originally applied to very thin substrates ($h \approx 0.1\%$ of the wavelength in the substrate) and overestimates patch width for thick substrates [41].

A variety of feeds can be implemented to excite a resonant patch from a microstrip transmission line. An exposed feed network can be printed on the same copper layer as the patches for a low-cost and simple solution with inset feeds providing the necessary impedance matching between the feed microstrip and patch microstrip, but this approach is not generally suitable for electronically steered arrays: interaction between the feed network and the radiating patches exacerbates mutual coupling and the scattering matrix formalism employed in this work does not allow for mutual coupling between a uniform array and the non-uniform feed network.

Feeding the patch from below the ground plane provides the necessary isolation between the array element and feed network and leaves space to integrate amplifiers and other active components. Connection between the feed network and patch through the ground plane can be achieved by a direct electrical conductor (probe-fed patch), or through a coupling aperture [42].

In this work, a linearly polarized rectangular patch with an air dielectric, suitable for HRIT reception (carrier frequency $f_c = 1694.1$ MHz, $\lambda_c = 176.96$ mm) was selected for the initial hardware prototypes. This is sufficient to validate the unit cell model and finite array reconstruction before pursuing the more complex problem of a dual-purpose array supporting both RHCP for polar satellites and selectable linear polarization for geostationary satellites.

An air-spaced design allowed for rapid assembly and adjustment with sufficient structural integrity for static tests in a protected environment; substituting low-density, low-permittivity foam in the air gap to construct a bonded sandwich structure requires only small changes to the geometry. A rectangular coupling aperture was used in all prototypes to reduce the number of variables for optimization but more complex aperture shapes such as modified bowties can achieve sufficient coupling with reduced back-radiation [43].

3.3 Numerical optimization

Transmission line formulas for the rectangular patch served as a starting point for subsequent numerical optimization. Patch and feed geometries were optimized for a single isolated antenna, without subsequent numerical refinement in a periodic unit cell ($d_x = d_y = 0.5\lambda_c$) at broadside (infinite array approximation, equal phase). The subarrays fabricated in this work are also small enough to optimize in an explicit model,[3] but this approach does not scale up to the full-size array and explicit models of 2D-subarrays were only used for validation of measurements.

The patch elements for the first prototypes were not specifically optimized in an array environment as these prototypes were constructed only to validate numerical accuracy. A successful element design for the wide-scanning L-band array would require additional structures for mitigation of mutual coupling beyond what is achievable with numerical adjustments to the basic patch geometry. One auxiliary structure, an array of complementary split-ring resonators (CSRR), is introduced in Section 3.5 as a first attempt to address the dominant E-plane coupling between adjacent elements.

Four optimized geometries for an isolated patch antenna over a $2 \cdot \lambda_c = 353.9$ mm square ground plane are presented in Table 3.2. Core thickness[4] corresponds to four available stock sizes of dielectric foam sheet. Upper (patch) and lower (aperture and feed network) FR4 skins are modeled with dielectric constant $\varepsilon_r = 4.3$[5] and a measured thickness of 1.59 mm. Copper pours are 35 μm thick (1 oz). Coupling slot width was fixed at 2 mm. For the purpose of these prototypes, the patches are placed on the top surface of the upper FR4 skin; the thickness of the skin is in addition to the specified core thickness. A sectional view of the patch element layers is illustrated in Figure 3.2.

---

[3]Explicit in that all array elements are included in the model space, and not implied through boundary conditions.

[4]Following Section 3.2, the initial prototypes developed in this work use patch geometries numerically optimized with air ($\varepsilon_r = 1$) serving as the dielectric core.

[5]Confirmed by measurement in Appendix B.3.

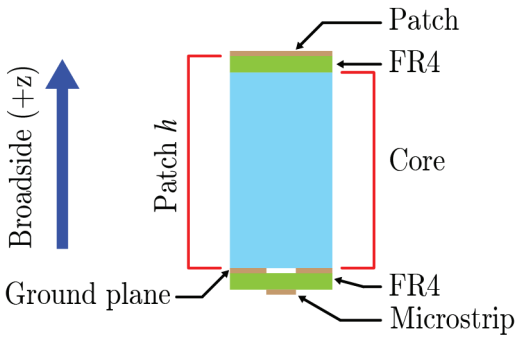

Figure 3.2: Sectional view of the layers in a patch element. The patch, ground plane, and microstrip transmission line are 1 oz copper, not to scale. Core material is air.

A commercial electromagnetics software package (CST Microwave Studio) provided the tetrahedral geometry meshing and the FDTD solver used to optimize geometry features. The goal function combined moving the local minimum of the reflection coefficient magnitude $|S_{11}|$ to f_c, maximizing the $|S_{11}| \leq -10$ dB bandwidth (VSWR ≈1.9:1), and minimizing the value of $|S_{11}|$ evaluated at f_c with a 2:2:1 weighting ratio as illustrated in Figure 3.3. The trust region framework optimizer, an algorithm based on successive linear models of the parameter space, was used to simultaneously refine patch length, patch width, coupling slot length, and the length of the impedance-matching stub on the 50Ω microstrip feed line to a local minimum.[6] The calculated 10 dB bandwidth of the reflection coefficient after optimization is presented in Table 3.2.

From this result, the 19.1 mm core thickness was selected for the subarray prototypes on the basis of reduced physical patch length, increased sandwich panel rigidity, and marginally increased bandwidth compared to a 12.7 mm core. The width of the patch (82.6 mm) is large compared to the desired array element spacing ($\Delta_{x,y} = 0.5\lambda_c = 88.5$ mm), but the performance of the isolated element is not very sensitive to modest reductions in width. For the subarray prototypes, the patch width was arbitrarily reduced by 20 mm and the geometry from Table 3.2 was then reoptimized

[6]Starting from the patch antenna with 12.7 mm core thickness in Table 3.2, a global optimization using a genetic algorithm did not discover another minimum with better goal function scoring after approximately 5,000 solver evaluations. Global optimization was not tested for other patch geometries due to high computational cost.

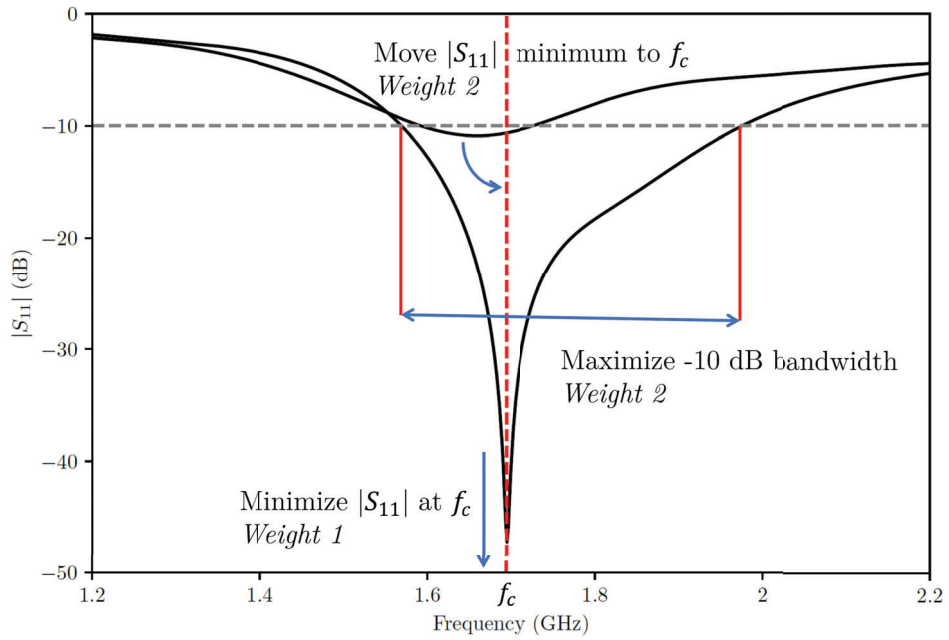

Figure 3.3: Weighted goal functions of the input voltage reflection coefficient magnitude $|S_{11}|$ used for all numerical optimization of patch antennas.

Core thickness	**Patch L**	**Patch W**	**Slot L**	**Stub L**	**Bandwidth**
7.9	60.2	83.9	39.0	5.95	213 MHz
12.7	59.4	87.2	44.0	6.53	372 MHz
19.1	51.8	86.2	48.4	4.04	396 MHz
25.4	48.3	81.0	50.9	3.27	264 MHz

Table 3.2: Critical dimensions (mm) and calculated 10 dB reflection coefficient bandwidth (MHz) for a single air-spaced rectangular patch antenna after numerical optimization. Geometry illustrated in Figure 3.4.

Core thickness	**Patch L**	**Patch W**	**Slot L**	**Slot W**	**Stub L**	**Bandwidth**
19.1	54.4	66.2	47.3	1.81	4.92	411 MHz

Table 3.3: Critical dimensions (mm) and calculated 10 dB reflection coefficient bandwidth (MHz) for an air-spaced rectangular patch used in subarray prototypes. Geometry illustrated in Figure 3.4.

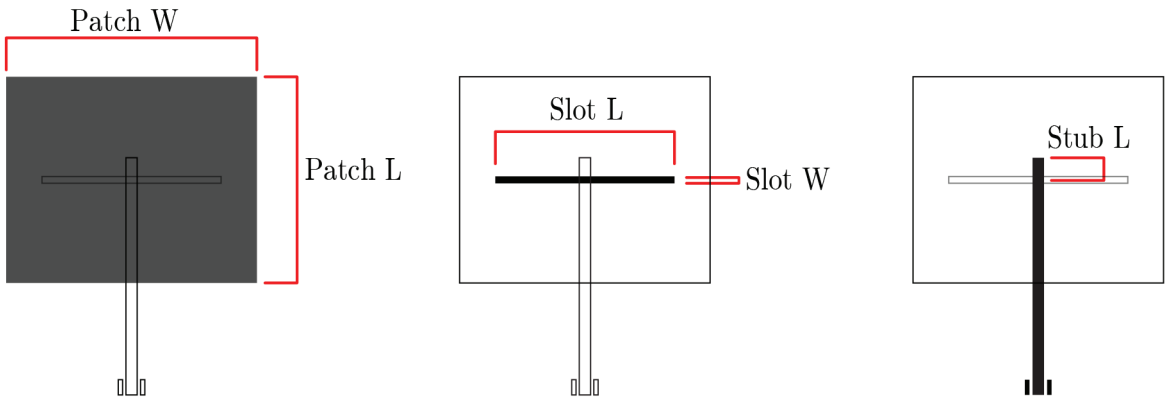

(a) Patch. (b) Slot aperture. (c) Microstrip feed.

Figure 3.4: Features in copper layers corresponding to the dimensions in Tables 3.2 and 3.3. The coupling slot is an aperture in a continuous ground plane. Stub L is measured from the center of the aperture. Copper pads for the SMA edge launch connector are described in Appendix B.2.

with fixed patch width. The coupling slot width, initially fixed at 2 mm, was also allowed to adjust. The final patch parameters, as used in all subarray prototypes, are listed in Table 3.3.

3.4 The finite array

Two minimum-size subarrays were designed to test model predictions of mutual coupling and embedded element behavior, constrained by the 202x271 mm maximum size of the fabrication process described in Appendix B. The 2×3 element subarray in Figure 3.5 orients the E-plane along the y-axis, and prioritizes sampling two unique E-plane scattering coefficients over one unique H-plane scattering coefficient between adjacent elements. A 2×1 element array was also fabricated as a subset of the 2×3 element array, placing elements 1 and 2 in Figure 3.5 on an enlarged ground plane to evaluate the dominant E-plane coupling in a minimum-size prototype with reduced edge effects. A third subarray prototype augmented the 2×1 element array with an E-plane decoupling structure described in Section 3.5.

All three subarrays were modeled explicitly with FDTD (time domain) and FDFD (frequency domain) electromagnetic solvers, without further refinement by numerical optimization. A selec-

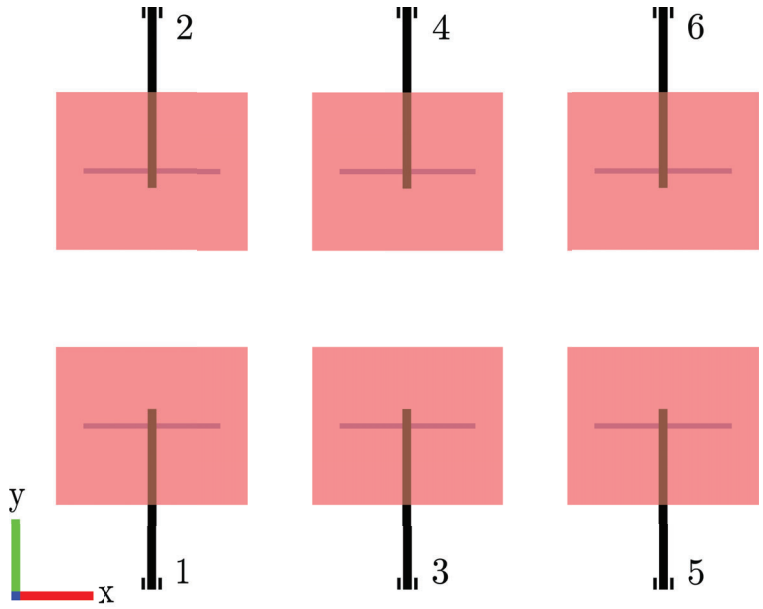

Figure 3.5: Geometry of a 2×3 element uniform rectangular array with port labels, viewed from broadside (+z). Element geometry features are illustrated in Figure 3.4. The beam steering vector is measured with angles θ from (+z), ϕ from (+x) toward (+y). Note that this feed geometry introduces an additional $180°$ phase shift by feeding the radiating slot aperture from opposite sides.

tion of modeled scattering coefficients for the 2×3 element array are presented in Figure 3.6; in all models, the magnitude of the scattering coefficient between E-plane adjacent elements exceeds the scattering coefficient between H-plane adjacent and diagonal-adjacent elements by 10-15 dB at $f = 1850$ MHz. Note that the reflection coefficient magnitudes $|S_{11}|$ and $|S_{33}|$ in Figure 3.6 assume all other elements are approximately match-terminated with 50Ω resistive loads, distinct from the active reflection coefficients in Figure 4.3 obtained by uniform excitation of the entire subarray.

Agreement between the time domain and frequency domain solvers is very close for the explicit model of the complete subarray.[7] In comparison, the scattering coefficients reconstructed from the active reflection coefficient in a periodic unit cell exhibit larger discrepancies, attributed more to the finite size of the ground plane than the absence of surrounding terminated elements in the

[7] As in Section 3.3, the explicit model contains the entire finite subarray geometry without any periodic boundary conditions.

explicit models. The phase shift between adjacent unit cells was scanned in 5° steps and the finite scattering matrix was reconstructed following the method in Section 2.3. The variable-phase periodic boundary condition in the unit cell propagates Floquet modes and necessarily requires a frequency domain solver [37].

A visual representation of the magnitude component of the complete scattering matrix at a single frequency $f = f_c$ is presented in Figure 3.7. Note that the reconstructed scattering matrix in Figure 3.7d depends only on the relative positions of elements in the array per Equation (2.5): all diagonal elements are identical, all adjacent E-plane couplings are identical, *etc.* In all versions of the scattering matrix for the 2×3 element array, the dominant off-diagonal term is E-plane coupling.

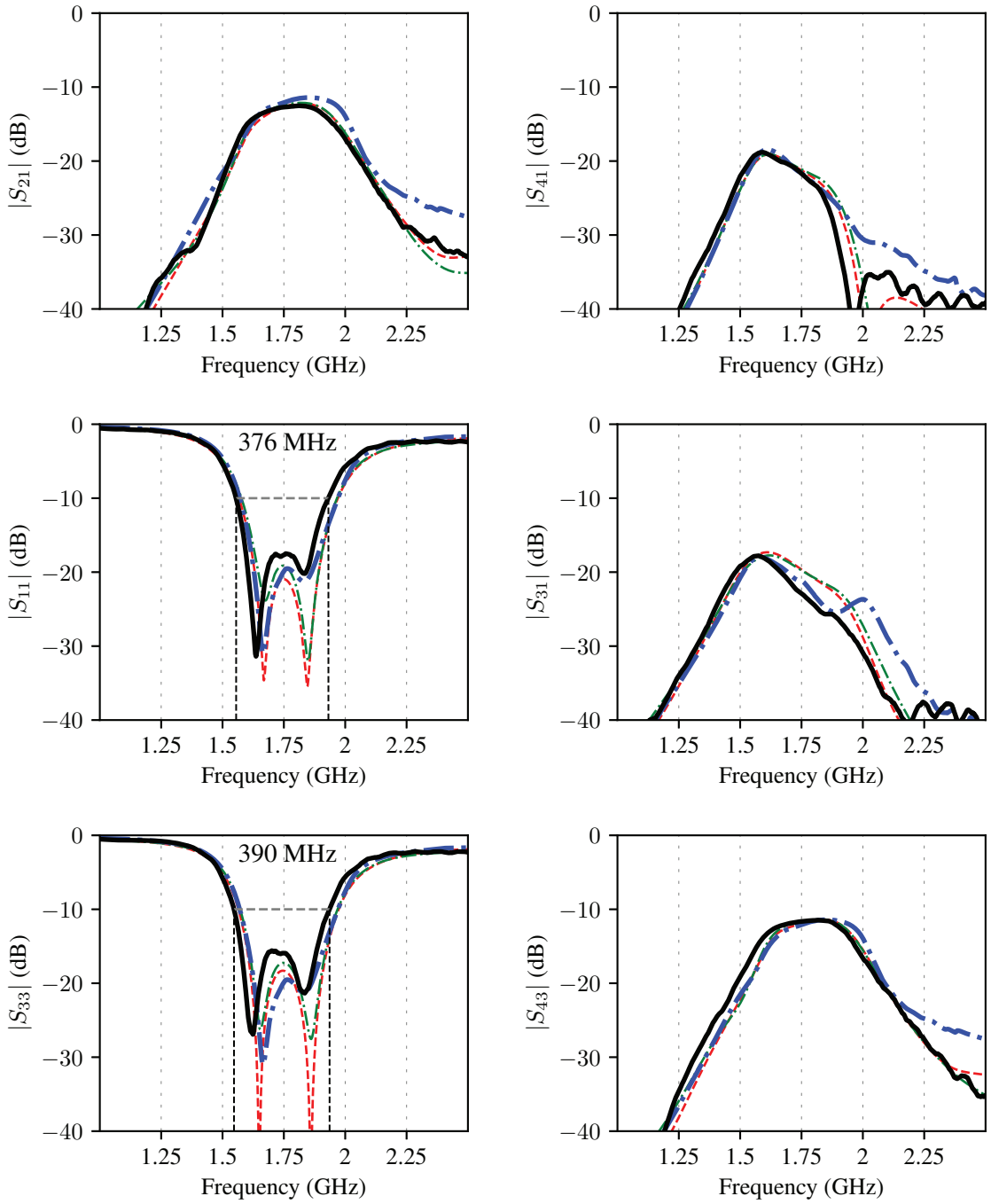

Figure 3.6: Measured — and modeled - - - magnitudes of the scattering coefficients for the 2×3 element array: corner $|S_{11}|$ and center $|S_{33}|$ element reflection coefficients; end $|S_{21}|$and center $|S_{43}|$ E-plane coupling; $|S_{31}|$ H-plane coupling; $|S_{41}|$ diagonal coupling. Models are explicit with time-domain solver ■, explicit with frequency-domain solver ■, and finite array reconstruction from a unit cell, frequency domain solver ■. $|S_{ii}| = -10$ dB bandwidths are indicated for the measured — magnitudes. Array element indices follow Figure 3.5.

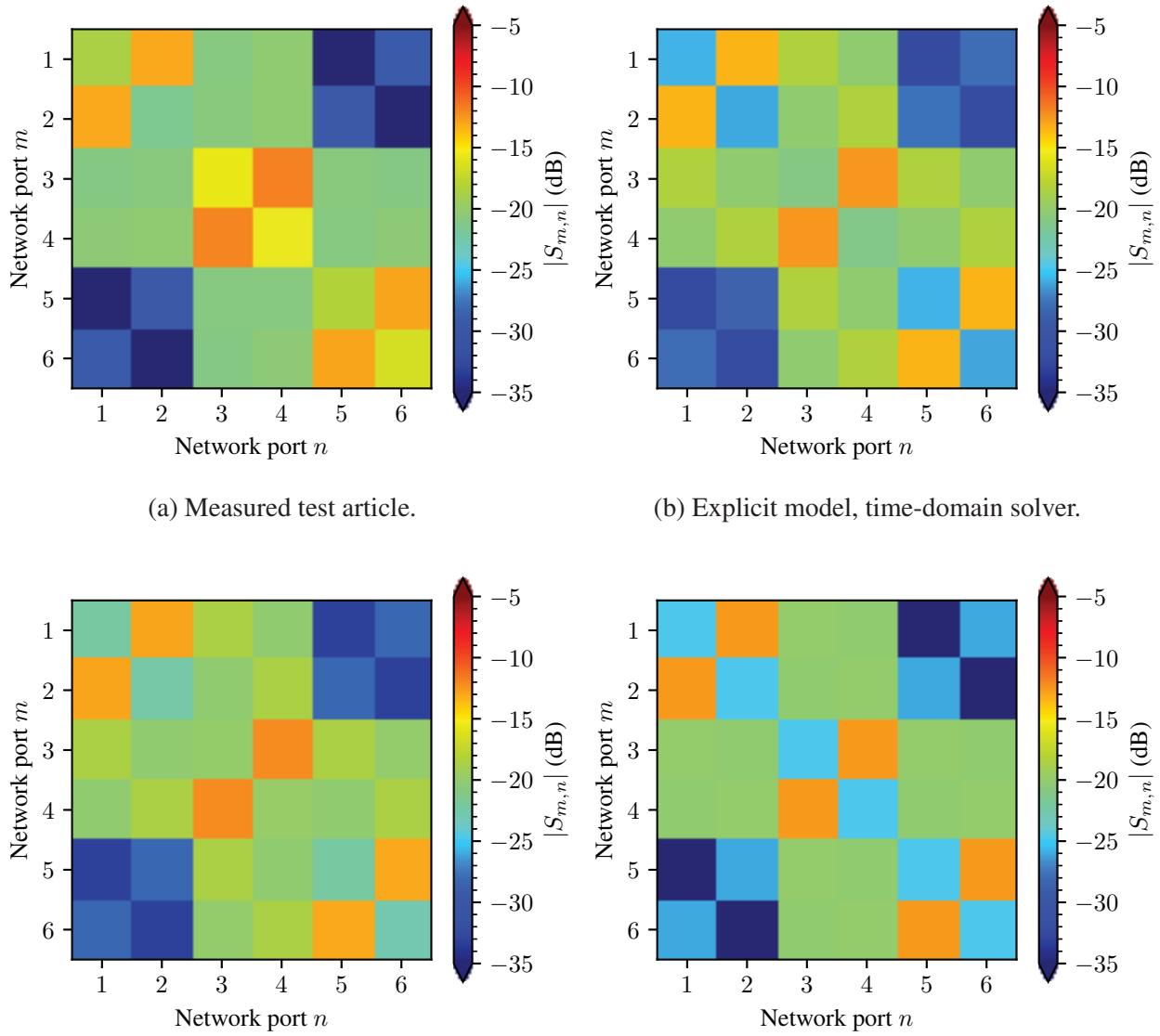

(a) Measured test article.

(b) Explicit model, time-domain solver.

(c) Explicit model, frequency-domain solver.

(d) Unit cell model reconstruction.

Figure 3.7: 6-port network scattering magnitudes $|S|$ at $f = f_c = 1694.1$ MHz for a 2×3 element uniform rectangular array. Network port indices follow Figure 3.5.

3.5 Mutual coupling mitigation

The 2×1 and 2×3 element subarray prototypes are simply arrays of isolated patch antennas; these are expected to exhibit strong E-plane coupling between adjacent elements. Following the transmission line model for a rectangular patch, each array element approximates a pair of slot antennas (magnetic dipoles) separated from the nearest slot antenna in an adjacent unit cell by $0.19\lambda_c$ in the E-plane and $0.13\lambda_c$ in the H-plane. As the ideal slot antenna has a pattern null along its axis (H-plane), the E-plane coupling between adjacent unit cells is expected to be the dominant mode of mutual coupling. In the same way, the mutual coupling between the feed apertures is strongest in the E-plane (separated by $0.5\lambda_c$).

The undesired couplings can be cancelled out by introducing an auxiliary coupling network with equal magnitude and opposite phase; this has been implemented with microstrip directional couplers for 1D arrays of probe-fed patch elements [44]. A directional coupler network for a 2D array would introduce significant complexity but could be extended from the 1D case for selective cancellation between E-plane adjacent elements in a 2D array.

An alternative approach to coupling mitigation introduces auxiliary resonant structures that interact with the array element instead of the feed network. A variety of miniature tuned resonators have been developed to electrically isolate adjacent elements. Simple microstrip structures, printed on the same layer as the radiating patch, include resonant linear microstrip transmission lines [45], more compact U-shaped microstrip transmission lines [46], and arrays of coupled, compact linear microstrip transmission lines [47].[8]

The patch element developed from Section 3.3 has a proportionally large substrate height of 19.1 mm $\approx 0.1\lambda_c$ and the substrate (air) has a low dielectric constant $\varepsilon_r \approx 1$. In this geometry, the coupling mechanism is predominantly near-field with little or no contribution from surface waves

[8] Shorting pins, grooved dielectrics, and defective ground plane structures are among the variety of other features used to reduce coupling between patch elements in beamforming and MIMO arrays; the suitability of a particular approach depends on desired element spacing, bandwidth, substrate dielectric constant, feed network compatibility, and other design variables [48].

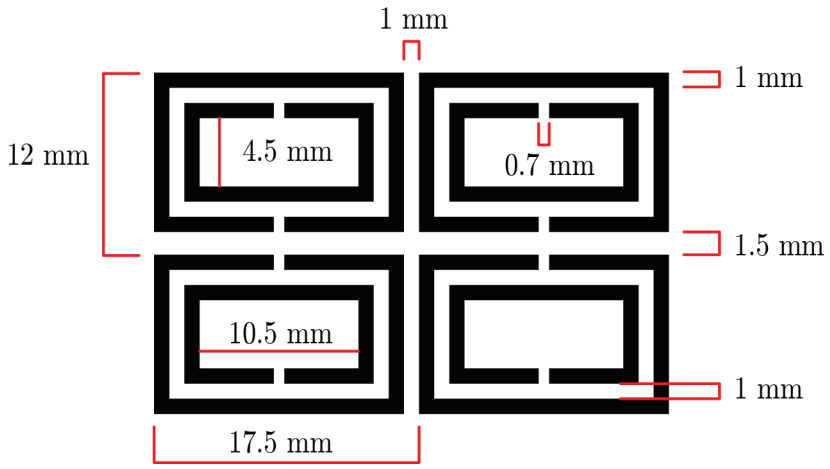

Figure 3.8: Critical dimensions of the complementary split ring resonator periodic structure unit cell. 2×2 unit cells illustrated.

and the electric field vector over the ground plane has a large vertical (z) component. Complementary split ring resonators (CSRRs), the complementary image of a split ring resonator etched into the ground plane, are both compact and resonant in a vertically polarized electric field [49]. Arrays of CSRR-derived structures between individual elements have been demonstrated previously [50].

In this work, a 2×5 element structure of nested complementary split ring resonators was placed at the array unit cell boundary. The resonator geometry in Figure 3.8 was hand-tuned within the explicit model of the 2×1 element array using a time-domain solver to resonate within the bandwidth of the patch element. The resonator geometry is not numerically optimized for bandwidth and limits the scale of fine features to ≈ 1 mm for reliable fabrication subject to the limitations in Appendix B.

This structure selectively reduces the E-plane coupling coefficient by ≥ 10 dB, as visualized by the surface currents on the ground plane in Figure 3.10, but the resonator is effective over only a narrow bandwidth in Figure 3.9b. Folding or other adjustment of the inner resonator may be required to broaden the effective decoupling bandwidth around the desired frequency $f = f_c$.

The reflection coefficient in Figure 3.9a is degraded across the element bandwidth, though remaining marginally below the -10 dB level. Numerical reoptimization of the radiating patch is likely required to compensate for loading by the CSRR structure.

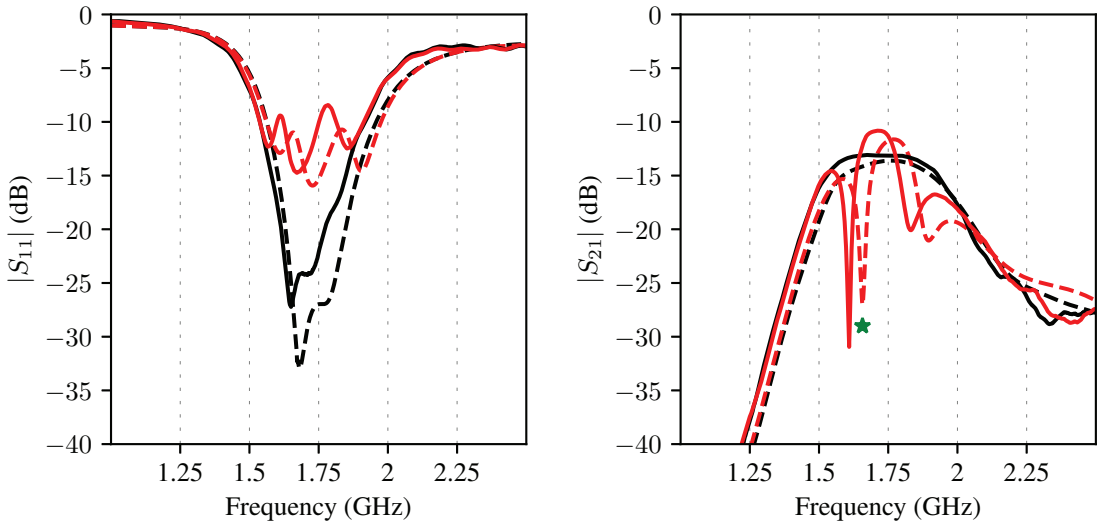

(a) Reflection coefficient S_{11}.

(b) Coupling coefficient S_{21}.

Figure 3.9: Measured ▬ and modeled - - - magnitudes of the reflection coefficient $|S_{11}|$ and E-plane mutual coupling coefficient $|S_{21}|$ for the plain 2×1 element array ■ and the array with CSRR ground plane structures ■.

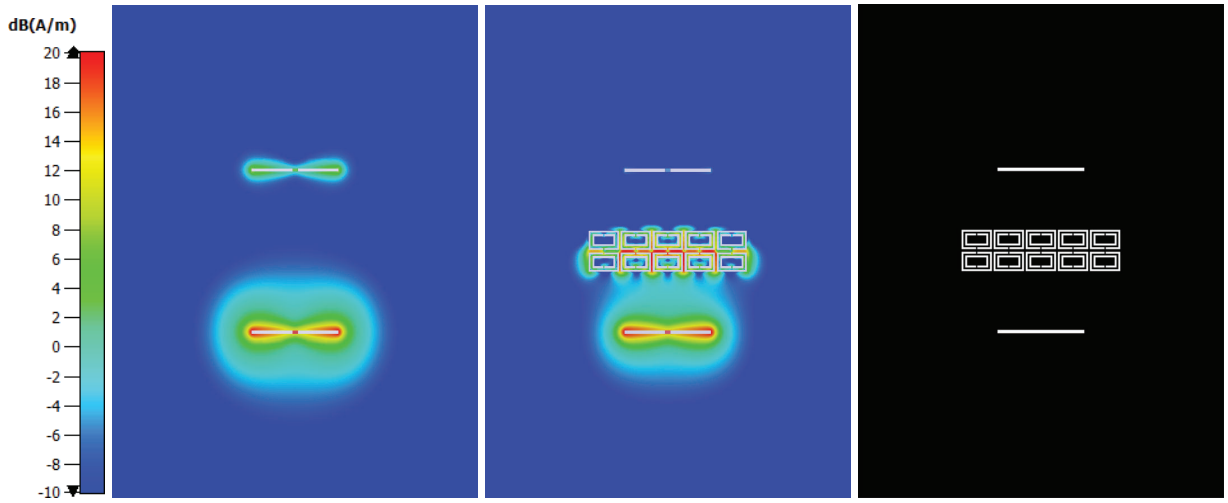

(a) 2×1 element array.

(b) Array with CSRR structure.

(c) Ground plane mask.

Figure 3.10: RMS surface current on the upper surface of the ground plane at ★1657 MHz, corresponding to the lower resonance in Figure 3.9b. Ground plane dimensions 200×270 mm.

CHAPTER 4

EMPIRICAL MEASUREMENTS

Scattering parameters and active element patterns were measured in an anechoic chamber at the University of New Hampshire. An Agilent E5063A vector network analyzer was used for all measurements. Practical aspects of fabricating and interfacing the prototype subarrays are described in Appendix B.

All coefficients of the scattering matrix for the 2×3 element array were measured independently regardless of symmetry; inactive array ports were terminated with 50Ω loads (Amphenol 132360). Active element patterns for two elements in the 2×3 element array were measured over the complete unit sphere with 3D positioner and a Vivaldi reference horn on a fixed tripod from Diamond Engineering. The free-space distance between the subarray under test and the reference antenna was measured within 3 mm using a laser rangefinder (Bosch GLM400CL). The test environment is illustrated in Figure 4.1. The provided reference horn gain calibration and calculated free space loss curves used to calibrate the active element gain measurements are illustrated in Figure 4.2.

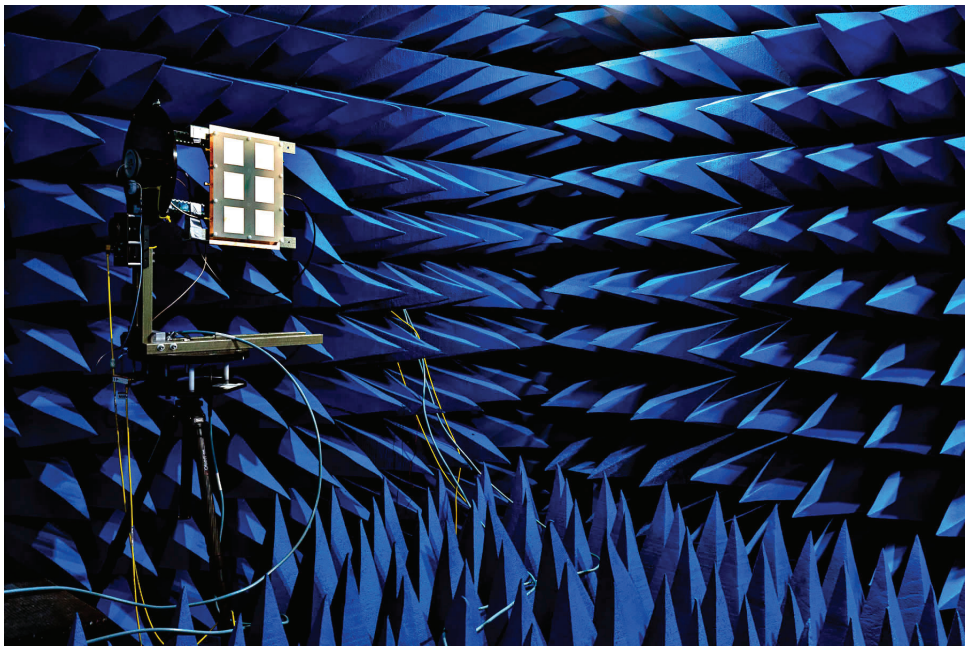

Figure 4.1: 2×3 element uniform rectangular array in the anechoic chamber.

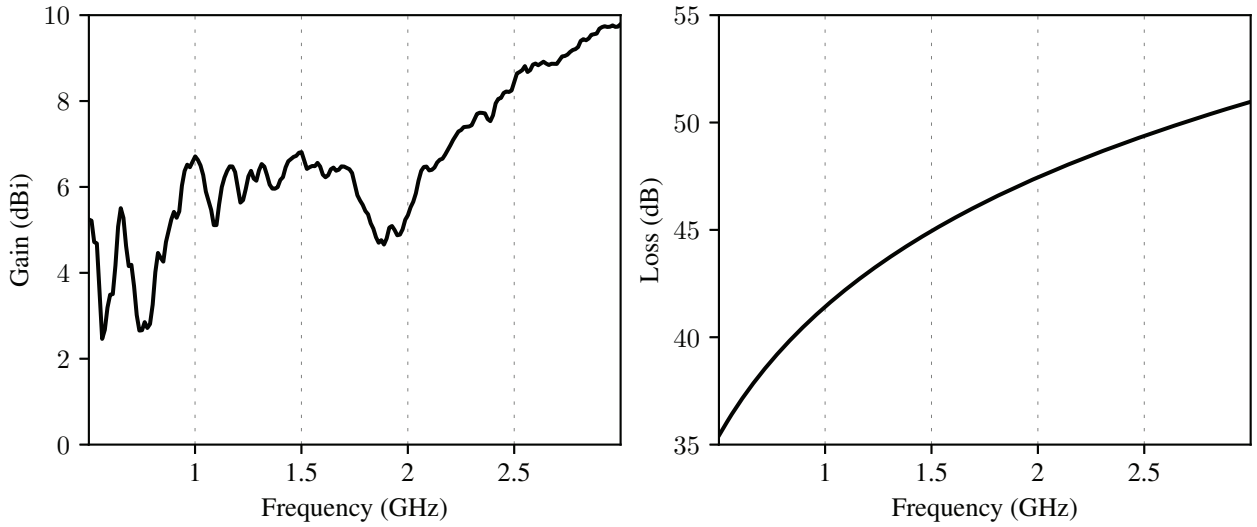

(a) Provided calibration, Vivaldi reference antenna.

(b) Free space loss, $d = 2.810$ meters.

Figure 4.2: Reference antenna gain and free space loss corrections for antenna pattern measurements.

4.1 Scattering matrix

Measured magnitudes of a selection of scattering coefficients from the 2×3 element array are presented in Figure 3.6 alongside explicit and reconstructed model predictions. Errors between coupling coefficients within the -10 dB bandwidth of the reflection coefficient are small, ≈ 2 dB for E-plane coupling and ≤ 5 dB for H-plane coupling, but the measured results exhibit a systemic shift to lower frequency.

A visual representation of the magnitude component of the complete scattering matrix at $f = f_c$ is presented in Figure 3.7a. Except for some violation of symmetry between $|S_{22}|$ and $|S_{55}|$, the structure of the scattering matrix with dominant E-plane coupling is consistent with numerical predictions. The reflection coefficients $|S_{ii}|$ are consistently larger than predicted at $f = f_c$, particularly for the middle array elements 3 and 4. This is evident in the corresponding frequency-domain plots in Figure 3.6.

Measured scattering coefficient magnitudes for the 2×1 element arrays in Figure 3.10 are consistent with the 2×3 element array: both element pairs closely follow the numerical models including the narrow resonances in the CSRR decoupling structure, but all features are shifted down in frequency. For the 2×1 element array with CSRRs, this shifts the lower resonance almost entirely outside of the numerically predicted bandwidth.

4.2 Active reflection coefficient

The active reflection coefficient encapsulates the core of the array design problem arising from mutual coupling.

By uniformly illuminating the scattering matrix of the 2×3 element array following Equation (2.3), the active reflection coefficients $S_{ii_{\text{active}}}$ were calculated for elements 1 and 3. This is visualized in the frequency domain for a selection of phase shifts in Figure 4.3.

The frequency domain plots, derived from the measured, explicitly modeled, and reconstructed scattering matrices, are consistent in two points: at broadside scan ($\varphi_{x,y} = 0$), the -10 dB band-

width is marginal compared to the reflection coefficient magnitudes in Figure 3.6, and the active reflection coefficients exhibit significant dispersion with phase shift. The measured and modeled results exhibit qualitative agreement but the discrepancies in magnitude are large compared to the reflection coefficients. This is not surprising, as the array has large coupling coefficients that combine constructively or destructively according to the phase shift.

The effect of this scan-dispersion on the array performance is illustrated in combined real (beam forming) and phase space for a selection of frequencies in Figure 4.4 at 1650 MHz, Figure 4.5 at $f = f_c = 1694.1$ MHz, and Figure 4.6 at 1900 MHz. Although the 0.5λ array element spacing was selected to accommodate a full scan angle range approaching $\theta = 90^\circ$ without grating lobes, both array elements have large blind areas in real space corresponding to increased reflected power. Consistent with Figure 4.3, there is qualitative agreement in the pattern of blind areas in real space predicted by the measured, explicitly modeled, and reconstructed scattering matrices, and the method of reconstructing the finite array scattering matrix from a periodic unit cell appears to be acceptable for predicting the scan performance of the array.

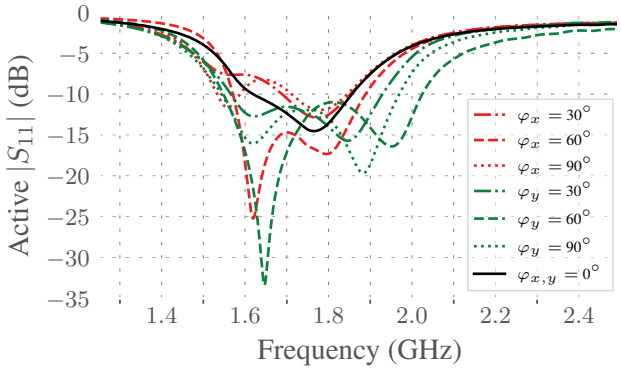

(a) Element 1, unit cell reconstruction.

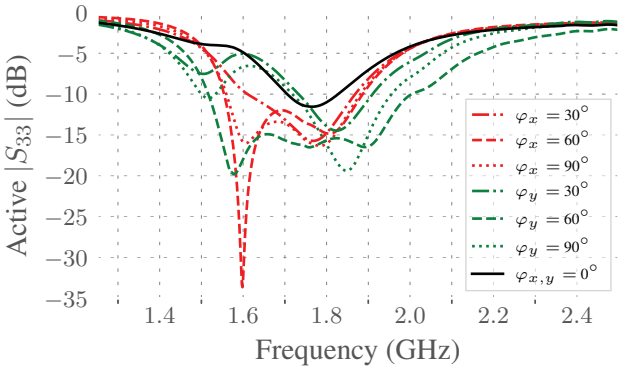

(b) Element 3, unit cell reconstruction.

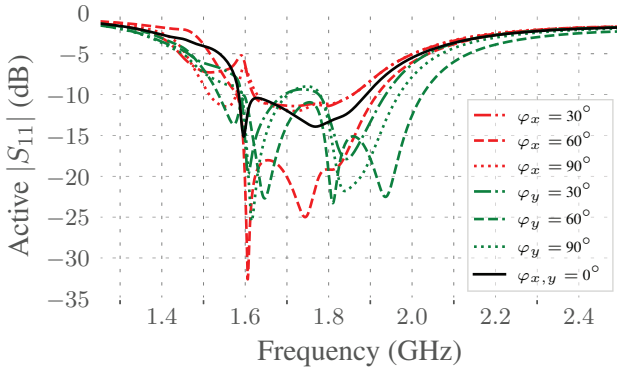

(c) Element 1, explicit model.

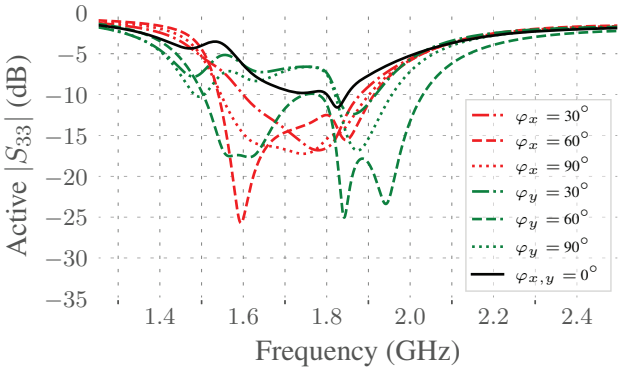

(d) Element 3, explicit model.

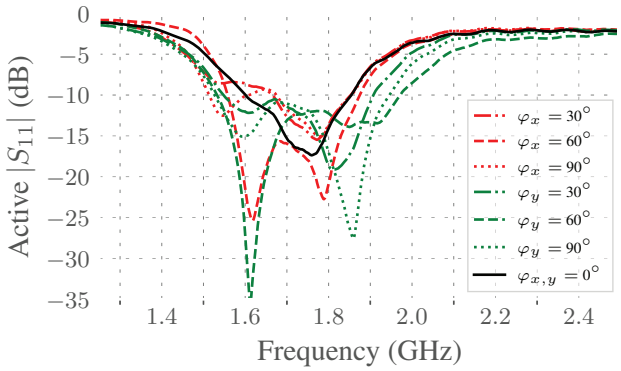

(e) Element 1, measured.

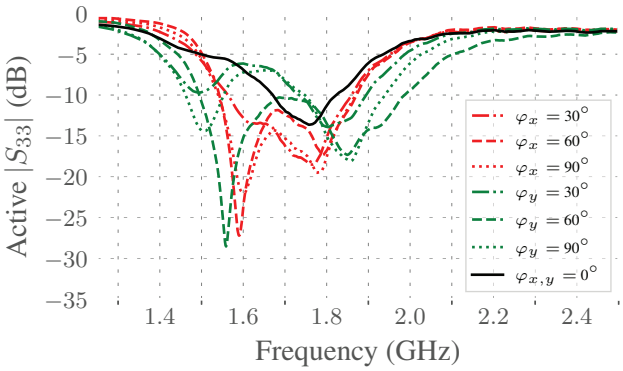

(f) Element 3, measured.

Figure 4.3: Scan-dispersion of the active reflection coefficient. Explicit numerical model using a time-domain solver.

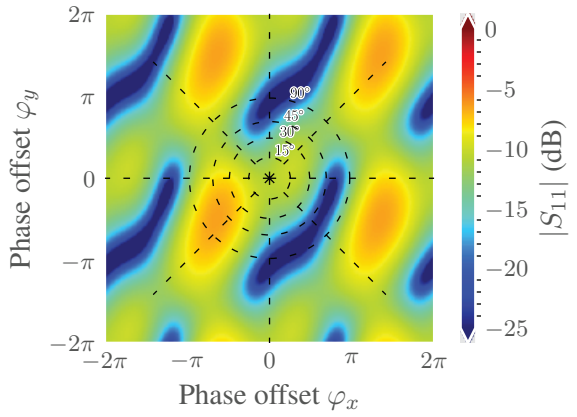

(a) Element 1, unit cell reconstruction.

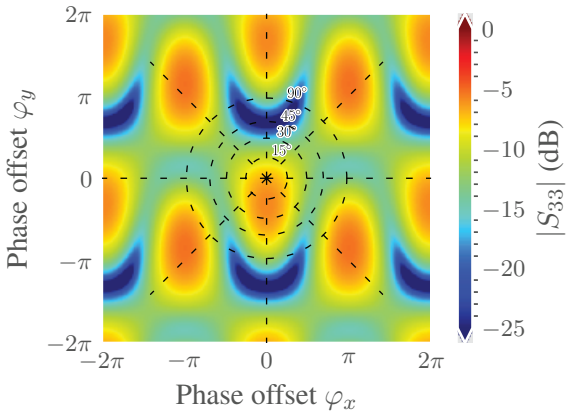

(b) Element 3, unit cell reconstruction.

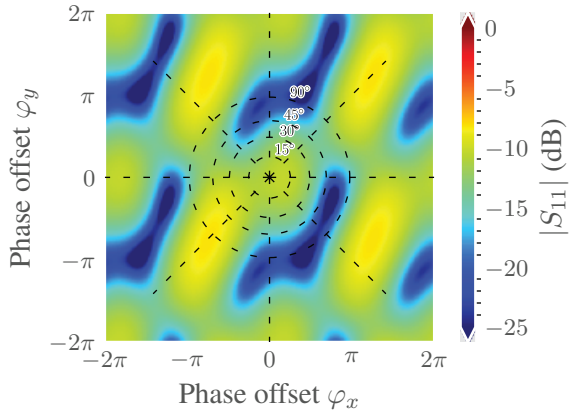

(c) Element 1, explicit model.

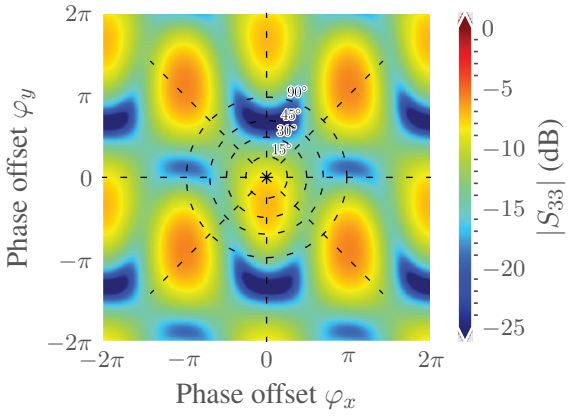

(d) Element 3, explicit model.

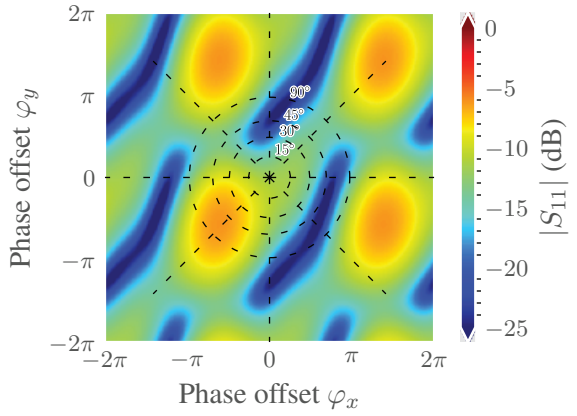

(e) Element 1, measured.

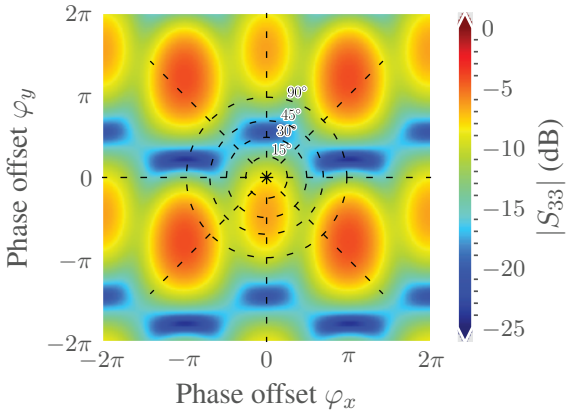

(f) Element 3, measured.

Figure 4.4: Circle diagrams of the active reflection coefficient for elements in the 2×3 array at $f = 1650$ MHz.

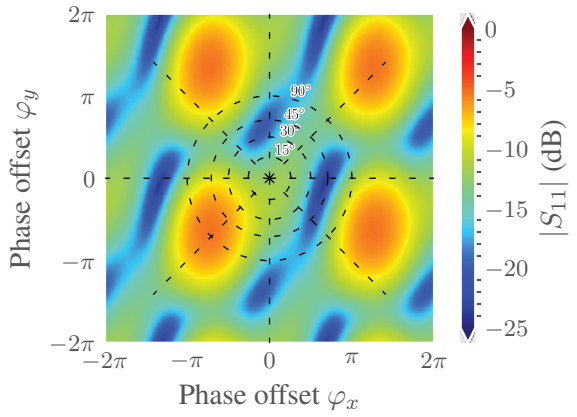

(a) Element 1, unit cell reconstruction.

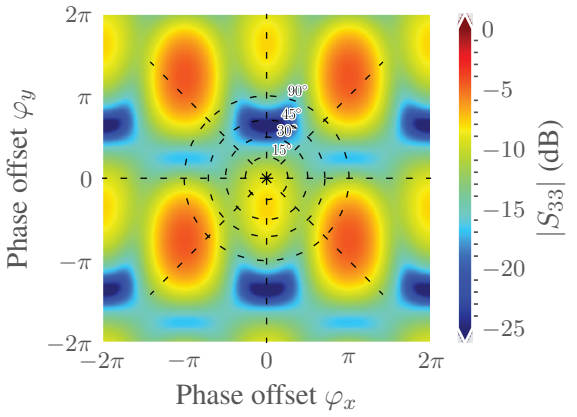

(b) Element 3, unit cell reconstruction.

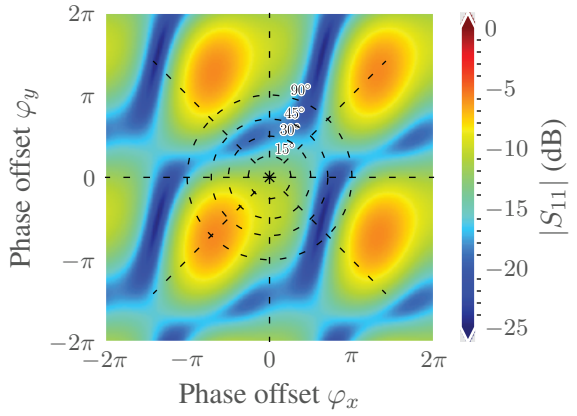

(c) Element 1, explicit model.

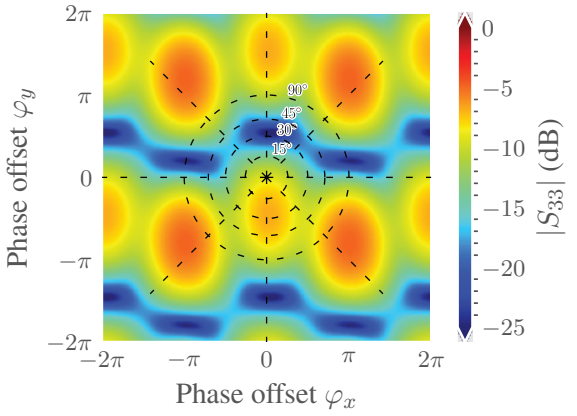

(d) Element 3, explicit model.

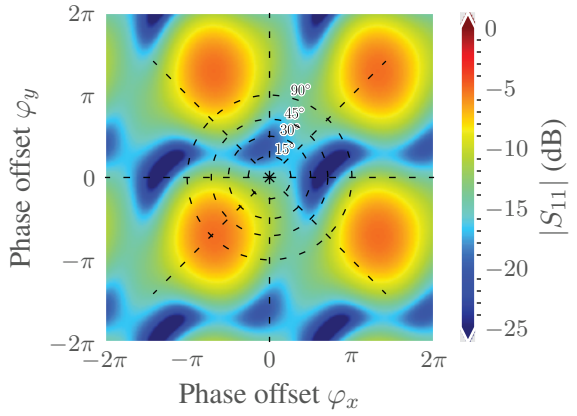

(e) Element 1, measured.

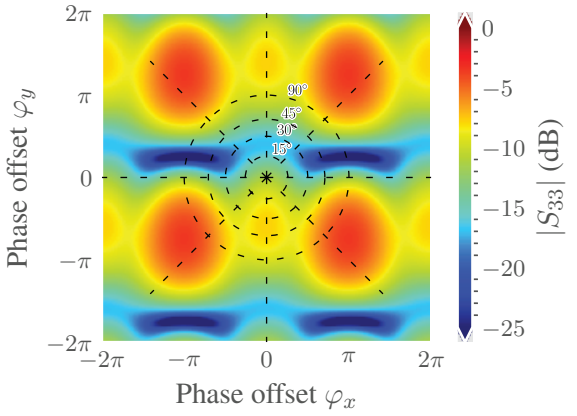

(f) Element 3, measured.

Figure 4.5: Circle diagrams of the active reflection coefficient for elements in the 2×3 array at $f = f_c = 1694.1$ MHz.

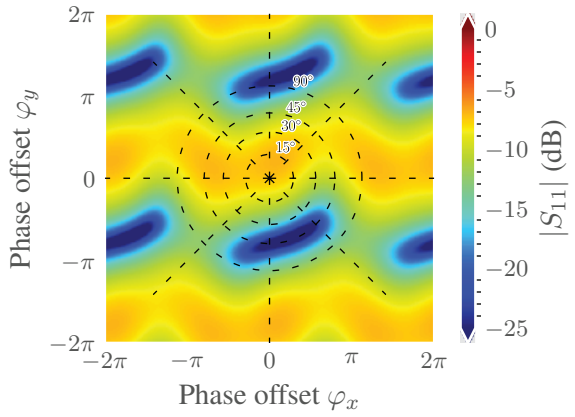

(a) Element 1, unit cell reconstruction.

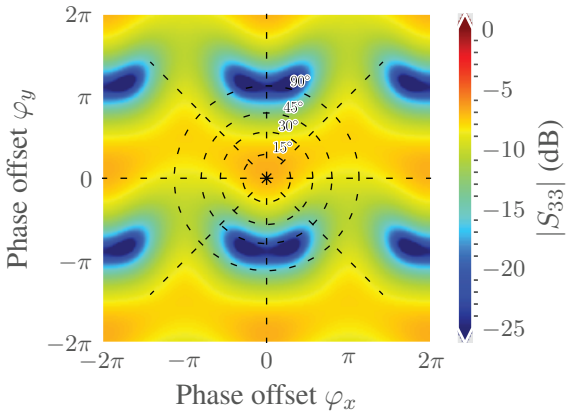

(b) Element 3, unit cell reconstruction.

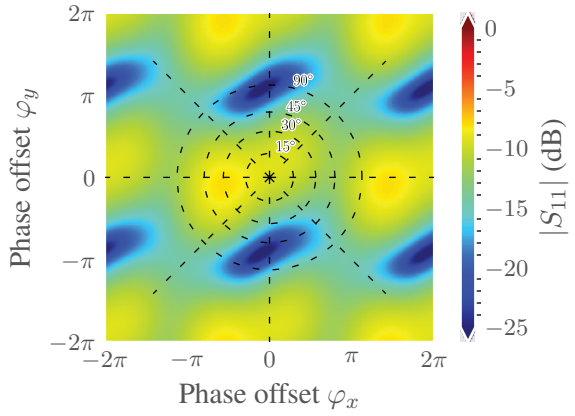

(c) Element 1, explicit model.

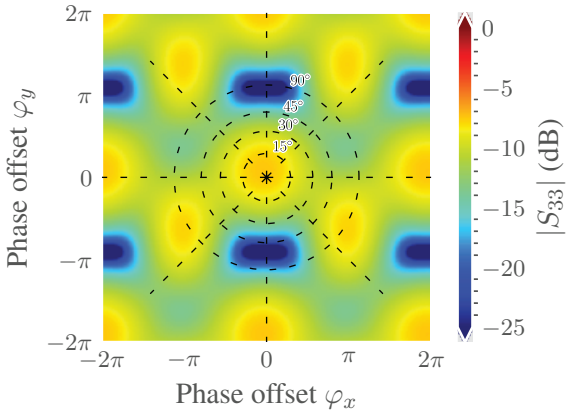

(d) Element 3, explicit model.

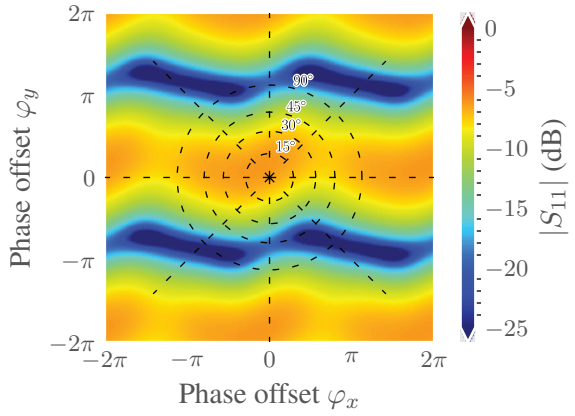

(e) Element 1, measured.

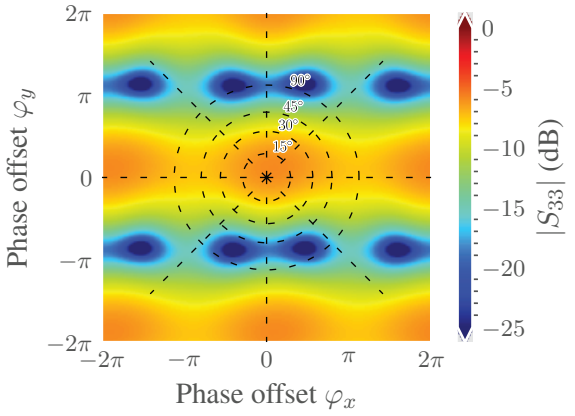

(f) Element 3, measured.

Figure 4.6: Circle diagrams of the active reflection coefficient for elements in the 2×3 array at $f = 1900$ MHz.

4.3 Active element pattern

The measured active element patterns for elements 1 and 3 at $f = f_c = 1694.1$ MHz are presented in Figure 4.8, following the element indices and axis convention in Figure 3.5. Corresponding E-plane and H-plane θ-cuts are illustrated in Figure 4.9. Frequency dispersion of the E-plane θ-cuts is illustrated in Figure 4.10 and H-plane θ-cuts in Figure 4.11.

Realized gain accuracy is generally acceptable in the unobstructed hemisphere ($\theta = 0 \pm 90°$) for the purpose of array pattern synthesis, but the lobes around $\theta = 30°$ predicted by the explicit model are not evident in the measured antenna pattern. Frequency dispersion of active element patterns follows the expected variation in reflected power, without significant change in pattern shape.

The accuracy of the measured back radiation from the coupling slots is degraded by supporting structure in the experimental measurement and exhibits generally larger discrepancies. As mounted on the positioner, the array was obstructed in the $+y$ direction ($\theta, \phi = 90°$) by a bearing and motor assembly adjacent to elements (2,4,6) as illustrated in Figure 4.7; this may account for the relatively large error around $\theta = 90°$ in Figure 4.9b. Combined with warping of the array layers described in Appendix B.1 and flexure in the physical mounting of the array, this impeded the accurate measurement of the nulls at $\theta = \pm 90°$. A supporting strip of duct tape was placed in the near field of elements (4,5,6) but influence on measurements of elements 1 and 3 is assumed to be minimal.

Although the patch elements were not optimized in an array environment, these preliminary active element patterns have sufficient gain ≥ 2 dBi for a finite array on the order of 200 elements with a maximum scan angle of approximately $\theta = 50°$ per Section 2.3 Footnote 3, with the exception of the element 3 H-plane cut: both the measured and predicted active element gains decrease to 0 dBi at $\theta = \pm 45°$ as illustrated in Figure 4.9d.

The two unique active element patterns obtained from the 2×3 array are valuable for comparison with finite array models, but they are not sufficient to predict the performance of a larger array. Interior and edge-adjacent elements will have different active element patterns reflecting

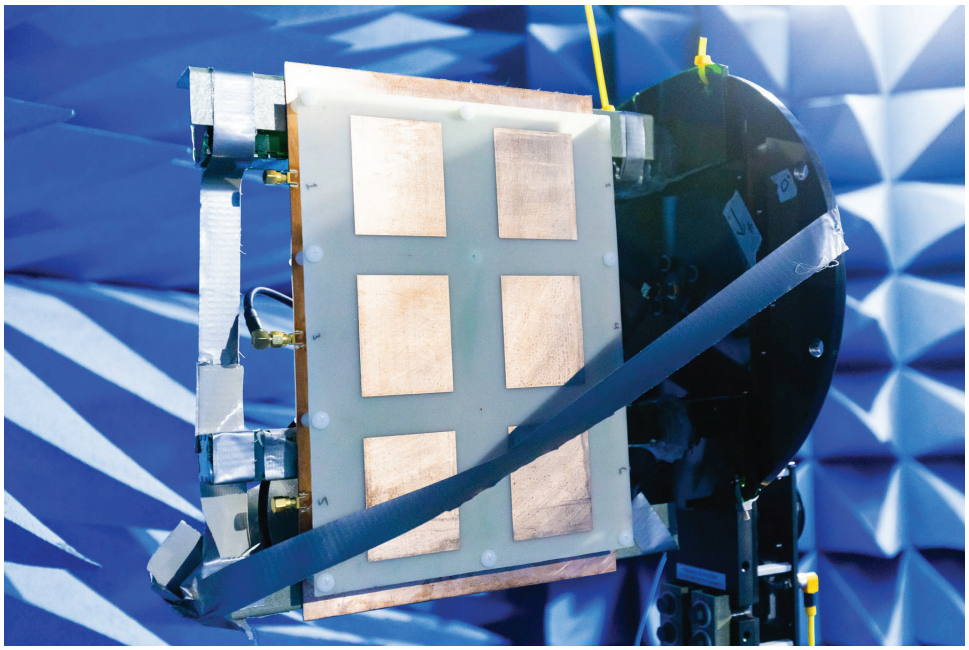

Figure 4.7: 2×3 element uniform rectangular array mounted for pattern measurement. The elevation axis bearing and motor assembly is adjacent to elements 2,4,6.

their unique coupling environments as compared to the corner and edge elements sampled here. Except for a polyhedron of small subarrays as described in Section 1.4, practical use of active element patterns for array pattern synthesis will require sampling elements from larger subarrays on the order of 10×10 elements following Section 2.3.

Following Section 2.2, the active element patterns can also be obtained from the active reflection coefficients. This was not attempted in this work but would be useful in evaluating the relative merit of measured active element patterns and active reflection coefficients for practical array performance prediction.

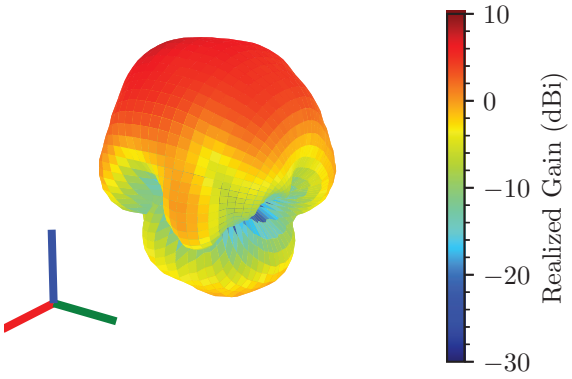

(a) Element 1 measured pattern

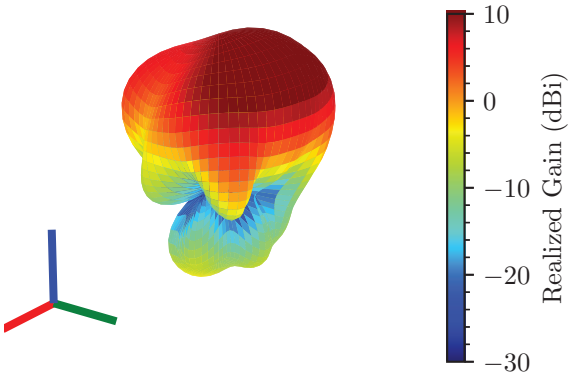

(b) Element 1 modeled pattern

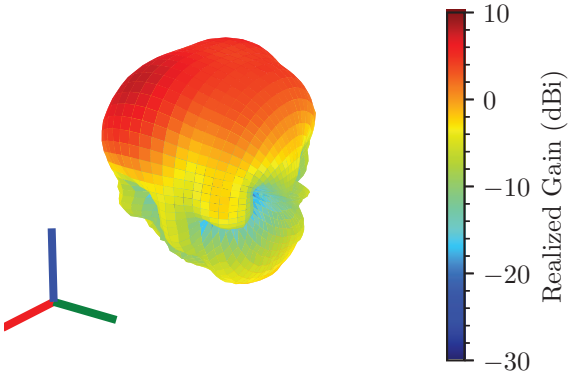

(c) Element 3 measured pattern

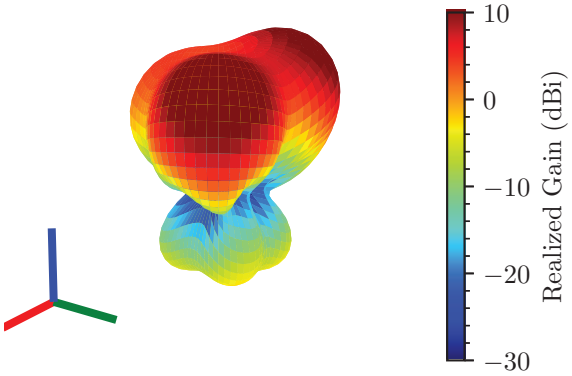

(d) Element 3 modeled pattern

Figure 4.8: Measured and modeled (frequency-domain solver) active element radiation patterns (realized gain) for the 2×3 element uniform rectangular array, $f = f_c = 1694.1$ MHz.

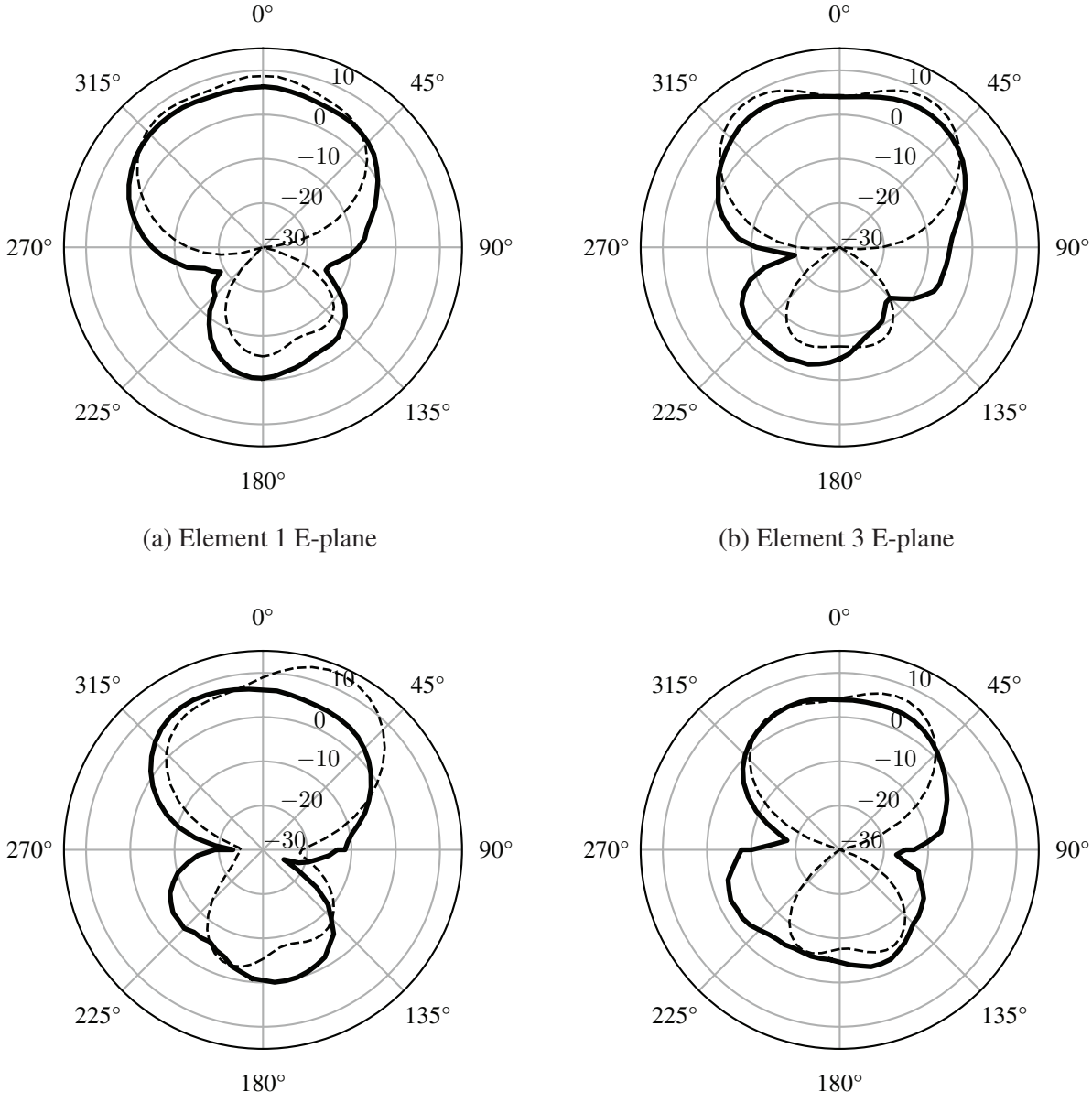

(a) Element 1 E-plane

(b) Element 3 E-plane

(c) Element 1 H-plane

(d) Element 3 H-plane

Figure 4.9: Measured — and modeled - - - radiation pattern θ-cuts for the 2×3 element uniform rectangular array, $f = f_c = 1.6941$ GHz. Radius is realized gain in dBi. Modeled results obtained with an explicit model and frequency-domain solver.

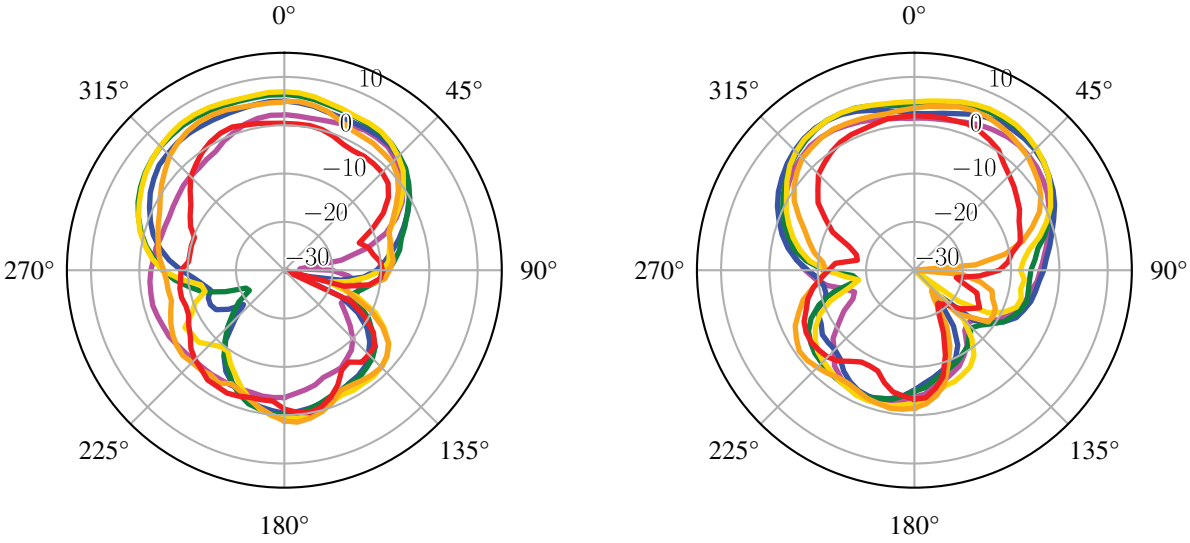

(a) Element 1, measured.

(b) Element 3, measured.

(c) Element 1, explicit model.

(d) Element 3, explicit model.

Figure 4.10: Measured — and modeled - - - E-plane θ-cuts for the 2×3 element uniform rectangular array, $f = 1.5$ GHz ■, 1.6 GHz ■, 1.7 GHz ■, 1.8 GHz ■, 1.9 GHz ■, 2.0 GHz ■. Radius is realized gain in dBi.

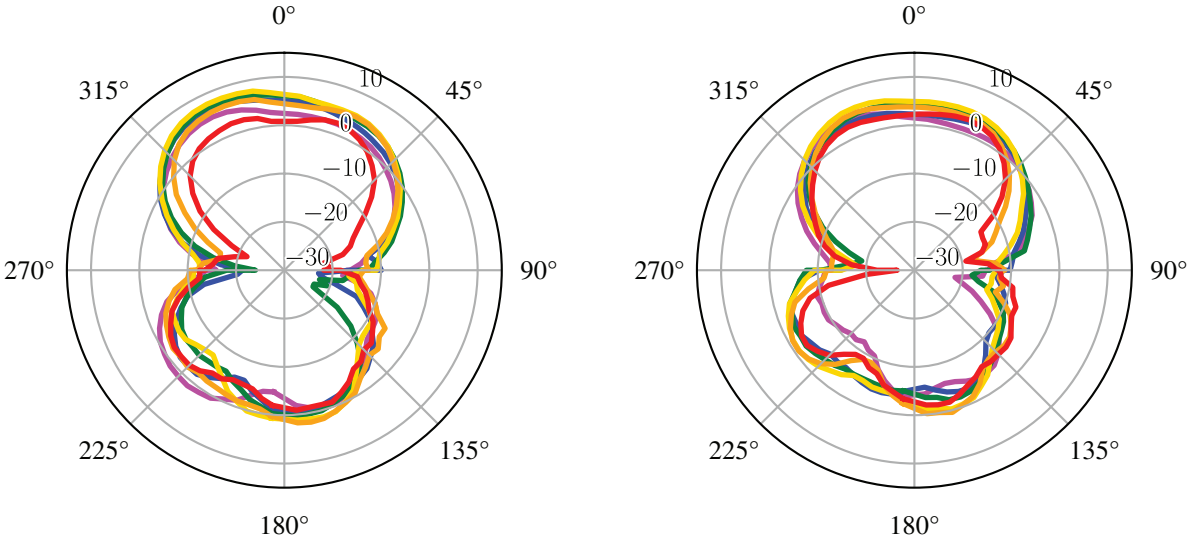

(a) Element 1, measured.

(b) Element 3, measured.

(c) Element 1, explicit model.

(d) Element 3, explicit model.

Figure 4.11: Measured — and modeled - - - H-plane θ-cuts for the 2×3 element uniform rectangular array, $f = 1.5$ GHz ■, 1.6 GHz ■, 1.7 GHz ■, 1.8 GHz ■, 1.9 GHz ■, 2.0 GHz ■. Radius is realized gain in dBi.

CHAPTER 5

CONCLUSION

This work presents the first steps in the process of designing a phased array antenna. The array designed, manufactured, and tested here demonstrates a viable workflow within the limits of numerical power.

Starting from a model in a periodic unit cell, the finite array scattering matrix was reconstructed with sufficient precision to capture the salient details of the active reflection coefficient. Scattering coefficients from explicit models of small subarrays were in good agreement with measured results, although a persistent frequency shift will need to be resolved when developing narrowband features. Small explicit models will be favored over single unit cell models for initial development of decoupling structures.

A successful design of a uniform planar array with large scan angle range will require designing extra measures to mitigate mutual coupling between elements before scaling up for the required array gain. How these auxiliary structures are best integrated, either in the feed network, ground plane, or the patch surface, should be the subject of further investigation.

BIBLIOGRAPHY

[1] World Meteorological Organization, "Observing Systems Capability Analysis and Review Tool," 2018. [Online]. Available: https://www.wmo-sat.info/oscar/

[2] "GOES-R Series Data Book," NASA GOES-R Series Program Office, Greenbelt, Maryland, Tech. Rep. CDRL PM-14, 2018.

[3] Z. Aijun, "Analysis on Specification of FY-3 Meteorological Satellite Data Transmission," *Journal of Applied Meteorological Science*, vol. 17, no. 4, pp. 494–501, 2006. [Online]. Available: http://html.rhhz.net/yyqxxb/html/20060486.htm

[4] EUMETSAT, "Metop Direct Readout AHRPT Technical Description," Tech. Rep. EUM/OPS/TEN/08/1663, 2021.

[5] ——, "Single Space Segment HRPT/LRPT Direct Broadcast Services Specification," Tech. Rep. MO-DS-ESA-SY-0048, 2000.

[6] "Report to the Maritime Safety Committee," International Maritime Organization, sub-committee on Navigation, Communications, and Search and Rescue, Tech. Rep. NCSR 8/14/1, 2021. [Online]. Available: https://docs.imo.org

[7] "Proposed Termination of U.S. Coast Guard Medium Frequency (MF) Broadcast of Navigational Telex (NAVTEX) and Shift to Satellite," *Federal Register*, vol. 84, no. 176, pp. 47 967–47 968, 2019.

[8] "NOAA N-PRIME Mishap Investigation Final Report," National Aeronautics and Space Administration, Tech. Rep., 2004.

[9] "User's Guide for Building and Operating Environmental Satellite Receiving Stations," National Oceanic and Atmospheric Administration, Tech. Rep., 2009.

[10] C. Bosquez, A. Ramos, and L. Noboa, "System for receiving NOAA meteorological satellite images using software defined radio," in *2016 IEEE ANDESCON*. IEEE, Oct. 2016, pp. 1–4. [Online]. Available: http://ieeexplore.ieee.org/document/7836233/

[11] A. Palosaari, *SDR FM demodulation*. linux-media mailing list, The Linux Kernel Organization, Feb. 2012. [Online]. Available: https://www.spinics.net/lists/linux-media/msg44103.html

[12] R. Aguilar-Gonzalez, A. Prieto-Guerrero, V. Ramos, E. Santos-Luna, and M. Lopez-Benitez, "A Comparative Study of RTL-SDR Dongles from the Perspective of the Final Consumer," in *2020 IEEE International Conference on Consumer Electronics (ICCE)*. IEEE, Jan. 2020, pp. 1–5. [Online]. Available: https://ieeexplore.ieee.org/document/9043161/

[13] A. Lahcen, "EUMETSAT – NOAA Collaboration in Meteorology from Space," European Space Policy Institute, Tech. Rep. 46, 2013.

[14] S. Gonnelli, A. Henrichs, and F. Thimler, "A data compression algorithm for the LRPT direct broadcast link on future polar orbit missions," in *IEEE 1999 International Geoscience and Remote Sensing Symposium. IGARSS'99 (Cat. No.99CH36293)*, vol. 4. IEEE, 1999, pp. 2026–2028. [Online]. Available: http://ieeexplore.ieee.org/document/775021/

[15] ITU-R, "Sharing of the 1670-1710 MHz band between the meteorological-satellite service and the mobile-satellite service," no. SA.1158-1, 1997.

[16] CGMS, "The Results of WRC-2000," Tech. Rep. CGMS-XXVIII USA-WP-14, 2000.

[17] U.S. Department of Commerce, "Identification of 15 Megahertz of Spectrum Between 1675 and 1710 MHz for Reallocation from Federal Use to Non-Federal Use Pursuant to Section 6401(a) of the Middle Class Tax Relief and Job Creation Act of 2012," Tech. Rep., 2013.

[18] WMO Commission for Basic Systems, "WMO Position on WRC-15 Agenda," 2014.

[19] P. Amirshahi and S. Grippando, "Radio frequency interference monitoring system for weather satellite ground stations: Challenges and opportunities," in *2017 IEEE International Symposium on Dynamic Spectrum Access Networks (DySPAN)*. IEEE, Mar. 2017, pp. 1–7. [Online]. Available: http://ieeexplore.ieee.org/document/7920780/

[20] P. Amirshahi, P. Ransom, S. Grippando, and I. Navarro, "Comparison of Centralized and Distributed Spectrum Monitoring Methods for Enabling Spectrum Sharing Between Weather Satellites and Terrestrial Networks," in *2019 IEEE International Symposium on Dynamic Spectrum Access Networks (DySPAN)*. IEEE, Nov. 2019, pp. 1–8. [Online]. Available: https://ieeexplore.ieee.org/document/8935816/

[21] Federal Communications Commission, "Report and Order," vol. 14-31A1, 2014. [Online]. Available: https://www.fcc.gov/wireless/bureau-divisions/broadband-division/advanced-wireless-services-aws

[22] P. Rocca, G. Oliveri, R. J. Mailloux, and A. Massa, "Unconventional Phased Array Architectures and Design Methodologies—A Review," *Proceedings of the IEEE*, vol. 104, no. 3, pp. 544–560, Mar. 2016. [Online]. Available: http://ieeexplore.ieee.org/document/7393660/

[23] Robert J. Mailloux, *Phased Array Antenna Handbook*, 3rd ed. Artech House, 2018.

[24] D. Loffler, W. Wiesbeck, M. Eube, K.-B. Schad, and E. Ohnmacht, "Low cost conformal phased array antenna using high integrated SiGe-technology," in *IEEE Antennas and Propagation Society International Symposium. 2001 Digest. Held in conjunction with: USNC/URSI National Radio Science Meeting (Cat. No.01CH37229)*, vol. 2. IEEE, 2001, pp. 334–337. [Online]. Available: http://ieeexplore.ieee.org/document/959731/

[25] M. Geissler, F. Woetzel, M. Böttcher, S. Korthoff, A. Lauer, M. Eube, and M. Wleklinski, "Phased Array for Maritime Satcom Applications," no. March, pp. 1–4, 2011.

[26] C. Balanis, "Antenna theory: a review," *Proceedings of the IEEE*, vol. 80, no. 1, pp. 7–23, 1992. [Online]. Available: http://ieeexplore.ieee.org/document/119564/

[27] D. M. Pozar, *Microwave Engineering*, 4th ed. Wiley, 2011. [Online]. Available: https://www.wiley.com/en-us/Microwave+Engineering%2C+4th+Edition-p-9780470631553

[28] P. Hannan, "The element-gain paradox for a phased-array antenna," *IEEE Transactions on Antennas and Propagation*, vol. 12, no. 4, pp. 423–433, Jul. 1964. [Online]. Available: http://ieeexplore.ieee.org/document/1138237/

[29] R. C. Hansen, *Phased Array Antennas*, 2nd ed., 2009.

[30] C. Craeye and D. González-Ovejero, "A review on array mutual coupling analysis," *Radio Science*, vol. 46, no. 2, pp. n/a–n/a, Apr. 2011. [Online]. Available: http://doi.wiley.com/10.1029/2010RS004518

[31] D. Pozar, "The active element pattern," *IEEE Transactions on Antennas and Propagation*, vol. 42, no. 8, pp. 1176–1178, 1994. [Online]. Available: http://ieeexplore.ieee.org/document/310010/

[32] D. M. Pozar, "A Relation between the Active Input Impedance and the Active Element Pattern of a Phased Array," *IEEE Transactions on Antennas and Propagation*, vol. 51, no. 9, pp. 2486–2489, 2003.

[33] H. Holter and H. Steyskal, "On the size requirement for finite phased-array models," *IEEE Transactions on Antennas and Propagation*, vol. 50, no. 6, pp. 836–840, Jun. 2002. [Online]. Available: http://ieeexplore.ieee.org/document/1017665/

[34] J. Lee, "G/T and noise figure of active array antennas," *IEEE Transactions on Antennas and Propagation*, vol. 41, no. 2, pp. 241–244, 1993. [Online]. Available: http://ieeexplore.ieee.org/document/214619/

[35] A. Roscoe and R. Perrott, "Large finite array analysis using infinite array data," *IEEE Transactions on Antennas and Propagation*, vol. 42, no. 7, pp. 983–992, Jul. 1994. [Online]. Available: http://ieeexplore.ieee.org/document/299601/

[36] A. K. Bhattacharyya, "Accuracy of Floquet Model in Predicting Performances of Finite Arrays," *IEEE Antennas and Wireless Propagation Letters*, vol. 13, pp. 19–22, 2014. [Online]. Available: http://ieeexplore.ieee.org/document/6692895/

[37] ——, *Phased Array Antennas*. Hoboken, NJ, USA: John Wiley and Sons, Inc., Dec. 2005. [Online]. Available: http://doi.wiley.com/10.1002/0471769126

[38] B. Lesur, A. Maati, M. Thevenot, C. Menudier, E. Arnaud, T. Monediere, C. Melle, D. Chaimbault, and A. Karas, "A Large Antenna Array for Ka-Band Satcom-on-the-Move Applications—Accurate Modeling and Experimental Characterization," *IEEE Transactions on Antennas and Propagation*, vol. 66, no. 9, pp. 4586–4595, Sep. 2018. [Online]. Available: https://ieeexplore.ieee.org/document/8399888/

[39] A. Johnson and G. Sims, "Mechanical properties and design of sandwich materials," *Composites*, vol. 17, no. 4, pp. 321–328, Oct. 1986. [Online]. Available: https://linkinghub.elsevier.com/retrieve/pii/0010436186907494

[40] C. A. Balanis, *Antenna Theory: Analysis and Design*, 4th ed. Wiley, 2016.

[41] M. Kara, "Empirical formulas for the computation of the physical properties of rectangular microstrip antenna elements with thick substrates," *Microwave and Optical Technology Letters*, vol. 14, no. 2, pp. 115–121, Feb. 1997. [Online]. Available: https://onlinelibrary.wiley.com/doi/10.1002/(SICI)1098-2760(19970205)14:2%3C115::AID-MOP12%3E3.0.CO;2-A

[42] D. M. Pozar, "A review of aperture coupled microstrip antennas: History, operation, development, and applications," *University of Massachusetts at Amherst*, no. May, pp. 1–9, 1996.

[43] V. Rathi, G. Kumar, and K. Ray, "Improved coupling for aperture coupled microstrip antennas," *IEEE Transactions on Antennas and Propagation*, vol. 44, no. 8, pp. 1196–1198, 1996. [Online]. Available: http://ieeexplore.ieee.org/document/511831/

[44] R.-L. Xia, S.-W. Qu, P.-F. Li, D.-Q. Yang, S. Yang, and Z.-P. Nie, "Wide-Angle Scanning Phased Array Using an Efficient Decoupling Network," *IEEE Transactions on Antennas and Propagation*, vol. 63, no. 11, pp. 5161–5165, Nov. 2015. [Online]. Available: http://ieeexplore.ieee.org/document/7236870/

[45] C. K. Ghosh and S. K. Parui, "Reduction of mutual coupling between E-shaped microstrip antennas by using a simple microstrip I-section," *Microwave and Optical Technology Letters*, vol. 55, no. 11, pp. 2544–2549, Nov. 2013. [Online]. Available: http://doi.wiley.com/10.1002/mop.27928

[46] S. Farsi, H. Aliakbarian, D. Schreurs, B. Nauwelaers, and G. A. E. Vandenbosch, "Mutual Coupling Reduction Between Planar Antennas by Using a Simple Microstrip U-Section," *IEEE Antennas and Wireless Propagation Letters*, vol. 11, pp. 1501–1503, 2012. [Online]. Available: http://ieeexplore.ieee.org/document/6387737/

[47] K. S. Vishvaksenan, K. Mithra, R. Kalaiarasan, and K. S. Raj, "Mutual Coupling Reduction in Microstrip Patch Antenna Arrays Using Parallel Coupled-Line Resonators," *IEEE Antennas and Wireless Propagation Letters*, vol. 16, no. c, pp. 2146–2149, 2017. [Online]. Available: http://ieeexplore.ieee.org/document/7918563/

[48] A. Christina Josephine Malathi and D. Thiripurasundari, "Review on Isolation Techniques in MIMO Antenna Systems," *Indian Journal of Science and Technology*, vol. 9, no. 35, Sep. 2016. [Online]. Available: https://indjst.org/articles/review-on-isolation-techniques-in-mimo-antenna-systems

[49] M. M. Bait-Suwailam, O. F. Siddiqui, and O. M. Ramahi, "Mutual Coupling Reduction Between Microstrip Patch Antennas Using Slotted-Complementary Split-Ring Resonators," *IEEE Antennas and Wireless Propagation Letters*, vol. 9, pp. 876–878, 2010. [Online]. Available: http://ieeexplore.ieee.org/document/5565383/

[50] A. Habashi, J. Nourinia, and C. Ghobadi, "Mutual Coupling Reduction Between Very Closely Spaced Patch Antennas Using Low-Profile Folded Split-Ring Resonators (FSRRs)," *IEEE Antennas and Wireless Propagation Letters*, vol. 10, pp. 862–865, 2011. [Online]. Available: http://ieeexplore.ieee.org/document/5995284/

[51] W. Pritchard, "The Calculation of System Temperature for a Microwave Receiver," in *The Communications Handbook*, 2nd ed., D. Gibson, Jerry, Ed. CRC Press, 2002, ch. 61, pp. 1–9.

[52] J. Roberson, E. Vallés, K. Tarasov, E. Grayver, and K. King, "A Flexible Software Based EMWIN/HRIT Prototype Solution for the GOES-R Transition," 2009.

[53] Qorvo, "Ultra Low Noise, Flat Gain LNA, TQL9092 datasheet," pp. 1–10, 2015. [Online]. Available: https://www.qorvo.com/products/d/da005305

[54] Peregrine Semiconductor, "UltraCMOS RF Digital Phase Shifter 8-bit, 1.7–2.2 GHz, PE44820 datasheet," pp. 1–22, 2018. [Online]. Available: https://www.psemi.com/pdf/datasheets/pe44820ds.pdf

[55] S. O. T. Land, O. Tereshchenko, M. Ramdani, F. Leferink, and R. Perdriau, "Printed circuit board permittivity measurement using waveguide and resonator rings," *IEEE International Symposium on Electromagnetic Compatibility*, vol. 2014-Decem, pp. 777–780, 2014.

[56] Cheng-Cheh Yu and Kai Chang, "Transmission-line analysis of a capacitively coupled microstrip-ring resonator," *IEEE Transactions on Microwave Theory and Techniques*, vol. 45, no. 11, pp. 2018–2024, 1997. [Online]. Available: http://ieeexplore.ieee.org/document/644224/

APPENDIX A

VESSEL MOTION AND LINK REQUIREMENTS

The two fundamental design parameters for the uniform rectangular array are gain and scan angle range. The gain of the antenna system, required to satisfy the link budget, and the maximum scan angle for the desired application together determine the size and layout of the array.

Neglecting the scan-dependent input impedance arising from mutual coupling between elements, the directivity of the array is the sum of the individual element directivities times the cosine of the scan angle from broadside (the ideal scan loss due to the shrinking projected aperture of the array) following Section 1.4. To a first approximation, the number of elements N in the array is directly proportional to the required directivity at the maximum scan angle θ_{max}, as the product of element gain, array gain, and scan loss.

Still neglecting mutual coupling between elements, the choice of element spacing Δ is a compromise between array directivity (proportional to Δ) and the emergence of grating lobes in real space for $\Delta > \lambda/2$. In a practical array, reducing the element spacing increases mutual coupling and can be constrained at a lower bound by the electrical size of individual array elements. A high-gain array with limited scan angle range is comparatively simple, as a large element spacing reduces mutual coupling and high-gain elements with low sidelobe levels can suppress grating lobes.

A.1 Link requirements

The link parameters for several L-band direct broadcast services are summarized in Table A.1. These links, and similar services from other geostationary and polar-orbiting weather satellites, occupy narrow bandwidths ($< 0.5\%$). A single antenna system with 1% bandwidth is sufficient to receive all available satellite signals.

To close the link, demodulate the signal, and decode the data payload, the ground station antenna system must receive the satellite signal with a minimum signal to noise ratio. Noise power at the feed point of the antenna system is a combination of noise generated within the antenna system by active and passive components, and received noise from external sources including radiated RFI and natural phenomena (sky background, certain astronomical objects, general blackbody radiation). Because the contribution from external noise sources is integrated over the antenna pattern, the additional noise power received by spurious features in the antenna pattern, such the back lobe, side lobes, and array grating lobes, degrades the signal to noise ratio at the antenna feed point. [40] This effect may be pronounced for satellite ground stations where the antenna main lobe is di-

	GOES-R HRIT	FenYun-3 CHRPT	MetOp-B/C AHRPT
Downlink f_c	1694.1 MHz	1701.4/1704.5 MHz	1701.3 MHz
Polarization	Linear	RHCP	RHCP
Minimum EIRP	56.8 dBm	41 dBm at 5°	31.5 dBm at nadir, 39.1 dBm at 60°
Modulation	BPSK FEC 1/2	QPSK FEC 3/4	QPSK FEC 3/4
Data rate	400 kbps	4.2 Mbps	3.5 Mbps
Symbol rate	927 kbps	5.6 Mbps	4.67 Mbps
Channel bandwidth	≥ 1.2 MHz	≥ 5.6 MHz	≥ 4.5 MHz

Table A.1: Representative examples of L-band direct broadcast services: GOES-R HRIT/EMWIN service [2], FenYun-3 CHRPT service [3], MetOp AHRPT service [4, 5].

rected toward a low-noise sky background, as the back lobe will be directed toward earth (a warm blackbody noise source) or possible sources of RFI.[1]

Allowing that the noise power spectrum is flat across the system bandwidth (white noise), a reasonable assumption for the narrow bandwidths in this work, noise power N is expressed as an equivalent noise temperature[2] T_e according to Equation (A.1):

$$N = kT_eB \tag{A.1}$$

where $k = 1.380 \times 10^{-23}$ is Boltzmann's constant in Joules/Kelvin or W/(K·Hz) and B is the system bandwidth.

The primary figure of merit for the antenna system is the gain to noise temperature ratio, G/T. As these satellite services are public broadcasts, detailed link budgets are available in the relevant technical documentation. For AHRPT broadcasts, EUMETSAT recommends a user station G/T of 6 dB/K, budgeting a link margin of 6 dB at all satellite altitudes $\geq 20^\circ$, degrading to 3 dB at 5° elevation above the horizon [5]. The minimum G/T required to close the link is then 0 dB/K for altitudes $> 20^\circ$. The HRIT link is required to close with a minimum G/T of -0.3 dB/K except at high latitudes [52].

As the minimum G/T ratio for both systems is approximately 0 dB/K, an array with a G/T ratio of 3 dB/K provides a reasonable link margin. Assuming an average noise temperature of 50 K from external sources, and low-noise amplifiers (1 dB NF) at every array element,[3] the per-element system noise temperature T is 50+75 K or 21 dBK. For a low-gain array element, G=2 dBi, the per-element G/T ratio is -19 dB/K. Allowing the array gain to scale with the number of elements

[1]Some variables in the link budget will act on both signal and noise. For example, rain attenuates the signal (increased path loss) and raises the received noise power relative to clear sky, both from the increased thermal noise of liquid water and by scattering other RF noise into the antenna aperture. [51]

[2]Also known as the brightness temperature.

[3]Economical L-band LNAs with noise figures less than 1 dB are available, such as the Qorvo TQL9092 with 0.65 dB NF [53].

N [34], 22 dB of array gain requires an array of at least 159 elements. This is satisfied by a 13×13 element array, before including scan loss.

If the array is scanned to $\theta = 50°$, the scan loss due to reduced projected aperture and impedance mismatch is estimated at 3 dB from Figure 1.4. Compensating with an additional 3 dB of array gain requires doubling the number of elements in the array, satisfied by an 18×18 element array. Larger scan angles are increasingly unfavorable unless some portion of the scan loss can be canceled by the active element pattern. Scan angles approaching or exceeding $\theta = 90°$ require a non-planar array geometry.

While this analysis is not rigorous, it is sufficient to establish an initial order-of-magnitude target for array size.

A.2 Scan range

The choice of element spacing $\Delta_{x,y}$ in the uniform array is a compromise between maximizing gain, minimizing coupling effects, and maximizing scan angle range.

Beam steering is required to track moving satellites and correct for vessel motion. The maximum required steering angle θ from broadside determines the maximum array element spacing, an important design parameter. Increasing element spacing reduces the undesirable near-field coupling between adjacent elements, relaxes constraints on the physical size of elements, and increases the nominal array aperture.

Considering a 1-D array, for element spacing $\Delta_x \geq 0.5\lambda$ and a particular phase shift, the elements of the array may combine constructively in more than one direction in real space. For a target beamforming angle θ_0, the spurious grating lobes emerge at angles θ_p subject to Equation (A.2):

$$\sin\theta_p = \sin\theta_0 \pm n\frac{\lambda}{\Delta_x} \tag{A.2}$$

where integers $n \neq 0$ satisfying $|\sin\theta_p| \leq 1$ correspond to real-valued grating lobe angles θ_p. To avoid grating lobes, the array element spacing has an upper bound given by Equation (A.3).

$$\frac{\Delta_x}{\lambda} \leq \frac{1}{1+\sin\theta_0} \tag{A.3}$$

For a polar-orbiting satellite, the beam steering range required to track a satellite pass is large; combined with vessel motion, a 2-D array capable of scanning an entire hemisphere is desirable and the array element spacing is fixed at $\Delta_{x,y} = 0.5\lambda$ for this work, a common choice for wide-scanning arrays [23]. Note that scanning the entire hemisphere to $\theta = 90°$ is not generally practical with a planar array due to scan loss.

If the application of the array is restricted to geostationary satellites and the array is manually repositioned after course changes, the required beam steering range is determined by the range of vessel motion. Three representative data sets collected from two vessels equipped with a suite of accelerometers, solid-state gyros, and magnetometers, is presented in Figure A.2 and Figure A.3. The desired pointing vector is at the center of the plot and the dots represent off-target pointing vectors perturbed by vessel motion. The $8.8°$ red circle corresponds to the 3 dB beamwidth of a parabolic dish with 24 dBi gain and a $\eta = 0.6$ efficiency factor, as suggested for a conventional

GOES HRIT ground station [9, p. 66]. All three samples follow the same basic parameters: the target satellite is at $40 - 45°$ altitude, $240 - 248°$ azimuth.

Dataset 'catamaran 1' was recorded in light wind and settled sea state, and pointing errors follow a slow yawing motion. Dataset 'monohull 1' was recorded under typical trade-wind reaching conditions, 15-20 knots wind speed and approximately 1.5 meter significant wave height. Under these conditions, the bow vector of the vessel traces an approximately helical pattern in time; as the monohull has less resistance to heel, the pointing error has a significant vertical component. Dataset 'catamaran 1' is recorded in an agitated sea state, with a measured significant wave height of 3 meters, resulting in the largest sample of high-slew rate data points in Figure A.3.

Note that other satellite azimuth values will result in different pointing error patterns under the same conditions; sample 'catamaran 1' is predominately yawing motion, 'monohull 1' has a large rolling motion, and 'catamaran 2' has a large and rapid pitching motion.

Taking these data sets as representative of the desired operating conditions, beam steering capability up to $20°$ from broadside is sufficient as illustrated in Figure A.1a. Considering only grating lobes, this would allow the element spacing to increase up to a maximum $\Delta_x = \Delta_y \simeq 0.74\lambda$ following Equation (A.3). Following Figure A.1b, a maximum beam slew rate of $15°/s$ is sufficient under these conditions. This is easily achieved with semiconductor phase shifters, for example the pSemi PE44820 with 25 kHz switching frequency [54].

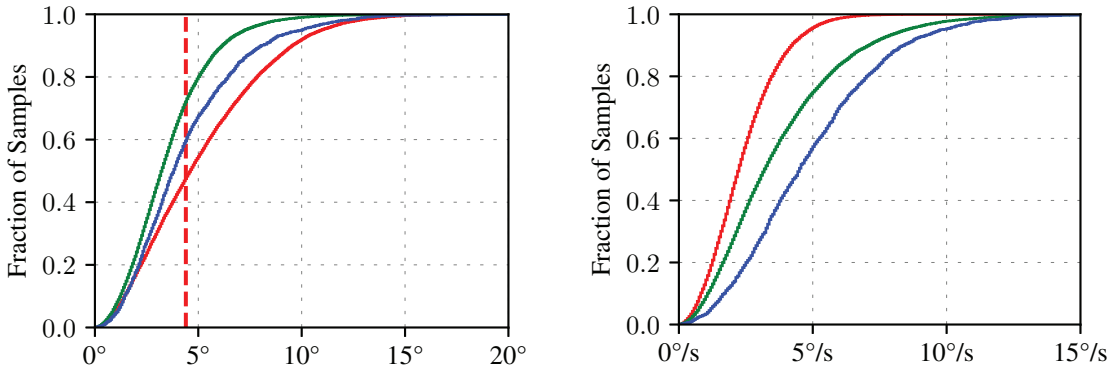

(a) Pointing error.

(b) Slew rate.

Figure A.1: Cumulative pointing errors and slew rates for catamaran 1 ■, monohull 1 ■, and catamaran 2 ■ motion data sets, summarized from Figures A.2 and A.3.

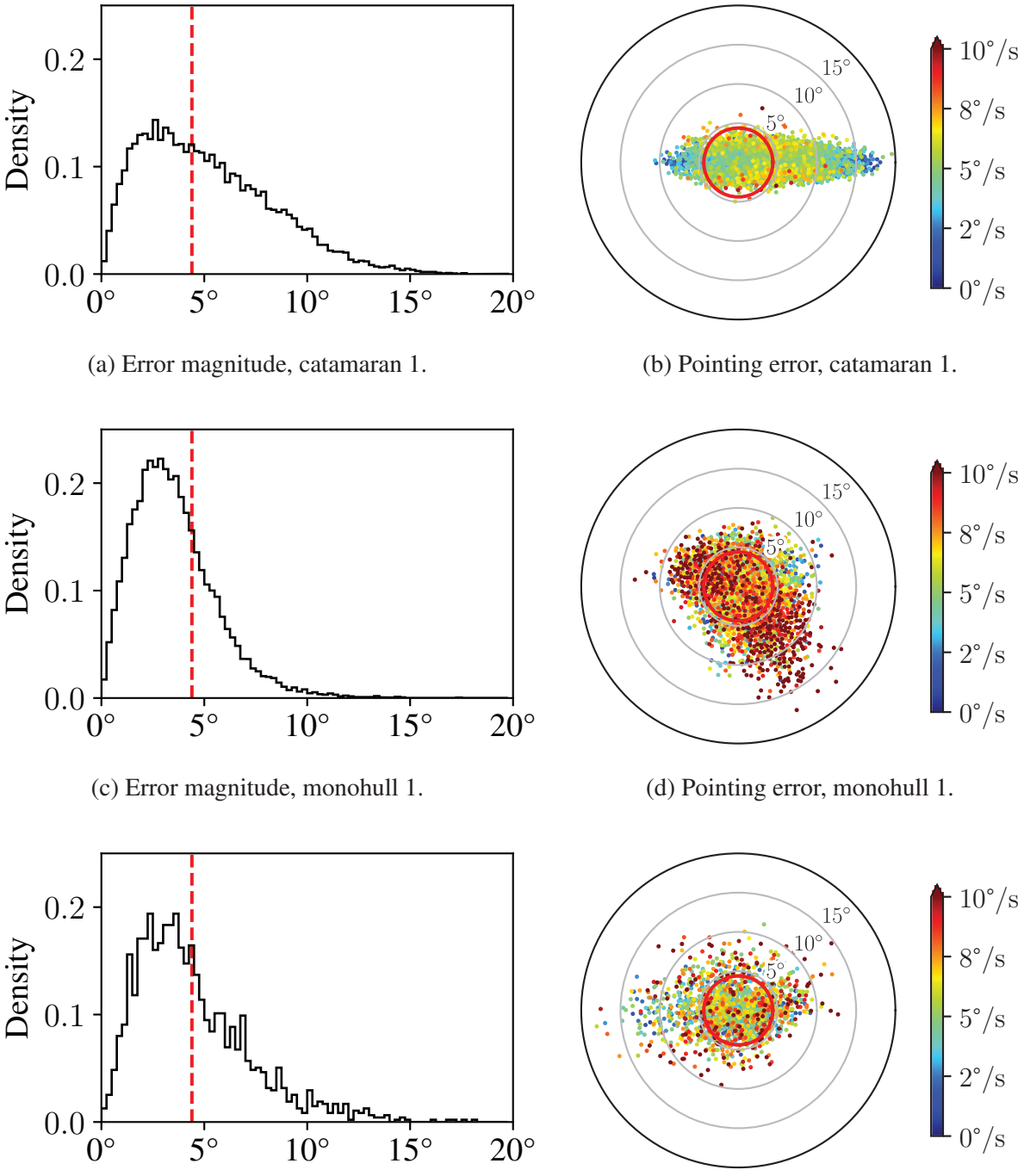

(a) Error magnitude, catamaran 1.

(b) Pointing error, catamaran 1.

(c) Error magnitude, monohull 1.

(d) Pointing error, monohull 1.

(e) Error magnitude, catamaran 2.

(f) Pointing error, catamaran 2.

Figure A.2: Vessel motion-induced pointing error magnitudes for GOES-East.

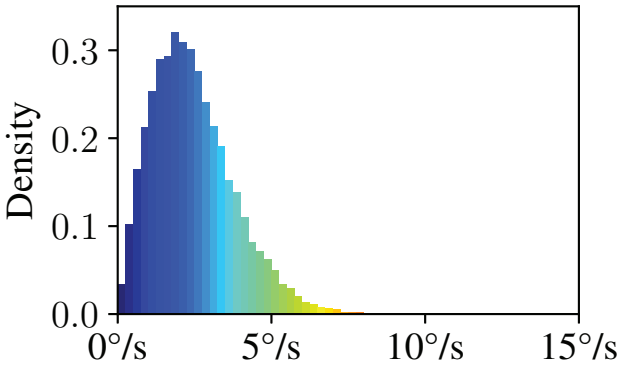

(a) Slew rate magnitude, catamaran 1.

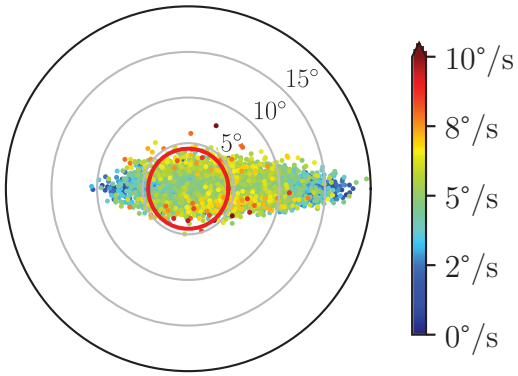

(b) Pointing error, catamaran 1.

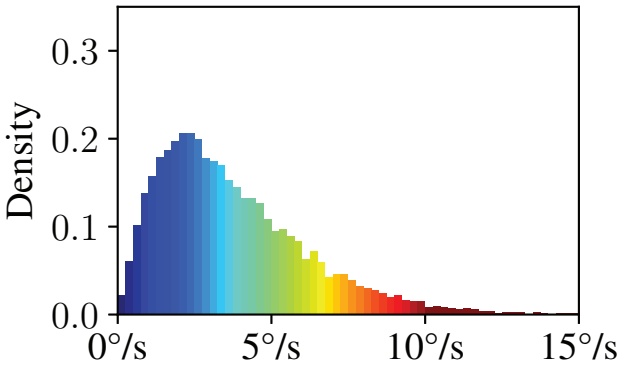

(c) Slew rate magnitude, monohull 1.

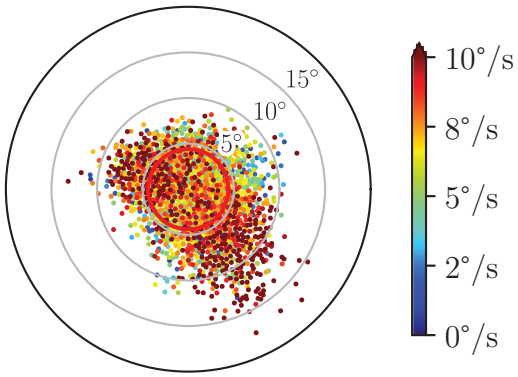

(d) Pointing error, monohull 1.

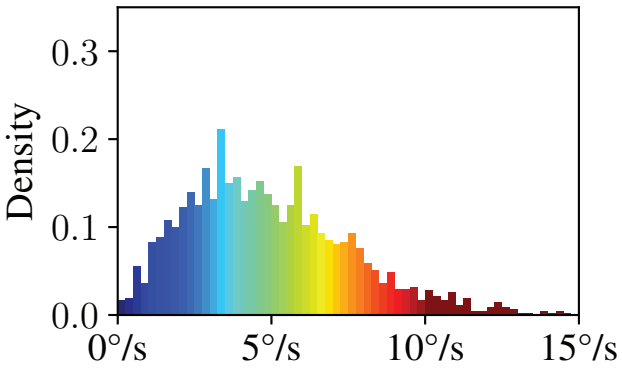

(e) Slew rate magnitude, catamaran 2.

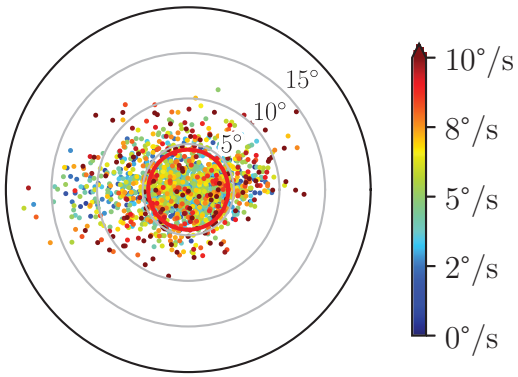

(f) Pointing error, catamaran 2.

Figure A.3: Vessel motion-induced pointing error slew rates for GOES-East.

APPENDIX B

FABRICATION OF SUBARRAYS

Test articles were fabricated from 1oz copper-clad sheets of FR4 composite via a conventional toner transfer process:

1. A consumer laser printer was used to pattern masks in toner (thermosetting plastic) on dextrose-coated transfer paper. Test patterns were used to calibrate the printer to within 0.07% dimensional accuracy in both axes.

2. The patterns were adhered to a clean copper surface with a combination of heat and pressure. A 12 mm-thick aluminum plate regulated by a PID controller and thermocouple served as a hot plate, and ink rollers were used to apply pressure to the transfer paper. Target conditions for transfer were $130°$C and 15 psi for 15 seconds. An initial pre-heat period mitigated pattern distortion from rapid drying of the transfer paper and warping from differential thermal expansion of the copper-clad FR4.

3. The copper-clad FR4 sheets were quenched in water and allowed to soak until the dextrose coating dissolved, releasing the transfer paper from the copper and pattern mask. The copper-clad FR4 sheets were then rinsed in clean water and allowed to air-dry.

4. Holes in the porous toner mask were sealed with a second toner-reactive plastic at $110°$C and 15 psi for 15 seconds.

5. Any remaining defects in the pattern were sealed with a resist pen. Large areas such as ground planes were sealed with a spray enamel.[1]

6. The exposed copper was etched to completion, typically 20-60 minutes subject to agitation, in a ferric chloride solution at $40°$C.

7. Etched sheets were rinsed in clean water and a saturated solution of sodium bicarbonate was used to neutralize any remaining etchant.

8. Toner and enamel masks were removed with acetone and lacquer thinner.

9. FR4 sheets were cut to final dimensions and edge launch SMA connectors were hot-air soldered.

---

[1] A marine engine spray enamel from Moller proved reliable and effective. Tests with waxes including synthetic mould wax and Carnauba wax did not reliably protect the copper surface from etching.

FR4 sheets with copper on both sides were processed in two separate operations, as simultaneously adhering patterns to two copper surfaces with controlled temperature and pressure was not reliable with the single heated plate. After etching one side of the substrate and masking the reverse side with spray enamel, the process was repeated with careful attention to moisture in the transfer paper and thermal warping of the substrate to ensure accurate registration. Although this fabrication process is not in general competitive with commercial PCB manufacturing services, it is suitable for this work because the subarray prototypes are physically large but do not require very fine features, through-holes, solder masks, and other operations included in commercial services that are typically priced per board area.

The minimum size for masked features was limited to 0.5 mm by the toner transfer process, but gap features down to 0.2 mm were reliably manufactured. Dimensional accuracy was 0.1% for dimensions up to 250 mm. Several models of laser printer were evaluated for resolution and artifacting, toner density, and toner tack temperature, before a Brother HL-5250DN was found acceptable. The maximum printable area for this printer was measured as 202x271 mm.

B.1 Array assembly

Figure B.1 illustrates the masking and etching process for the ground plane slot apertures in the 2×3 element array. Peripheral registration lines on the ground plane and transfer paper in Figure B.1a were used to align the toner mask with the microstrip feeds etched on the opposite side of the FR4 sheet. In Figure B.1c, the mask has been sealed with toner-reactive plastic, the edges of the ground plane are protected with spray enamel, and any remaining defects have been masked with a black resist pen. The slot apertures have been etched to completion and neutralized, and the ground plane is ready for solvent cleaning.

Following the patch element design in Section 3.2, the initial hardware prototypes were assembled from air-spaced FR4 sheets fastened with nylon bolts and 19 mm nylon standoffs. Through-bolted lengths of glass-filled polyester angle stock provided mechanical attachment to the test stand and additional stiffening for the lower FR4 substrate. The 2×1 element subarray in Figure B.2 is representative of both two-element prototypes. The 2×3 element subarray in Figure B.3 is oriented to match the reference layout in Figure 3.5.

This mode of assembly does not realize the stiffness of the bonded sandwich structure proposed in Section 3.1, and the subarray prototypes retained some flexibility after final assembly. A vacuum-laminated structure would guarantee flatness in the final assembly, while also requiring careful registration of the patch and feed substrates. In the scope of this work, the bolted, air-spaced arrays facilitated rapid assembly and allowed the option of substituting different patch substrates and feeds.

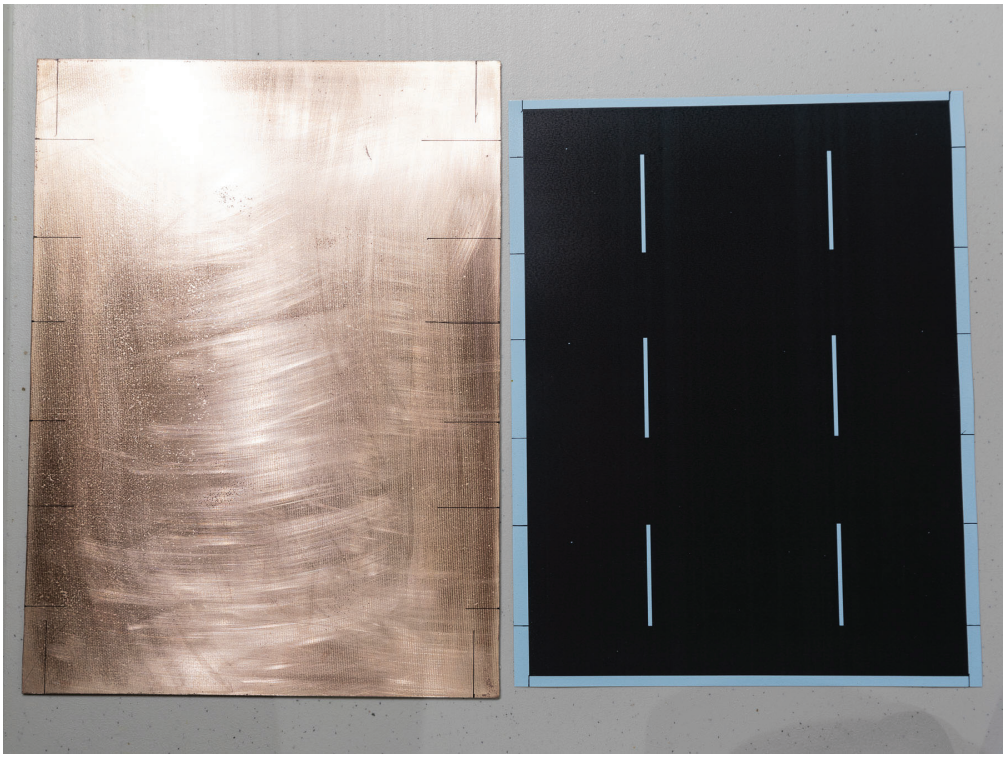

(a) Design printed on transfer paper.

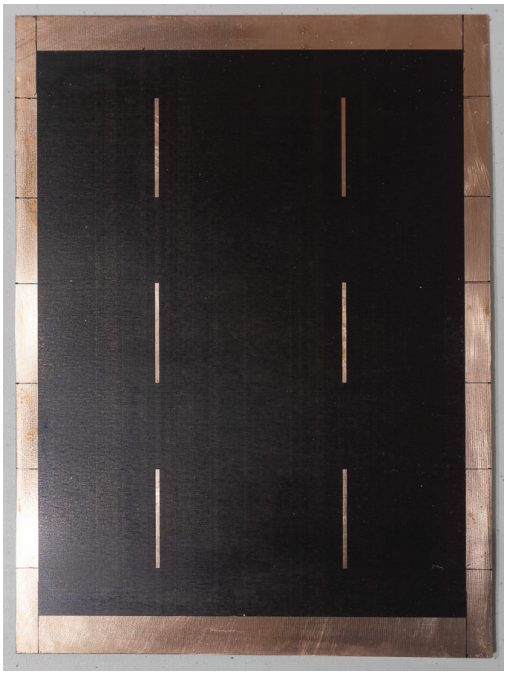

(b) Design on copper after toner transfer, not sealed.

(c) Design after sealing and etching.

Figure B.1: Fabrication of radiating slot apertures for the 2×3 array.

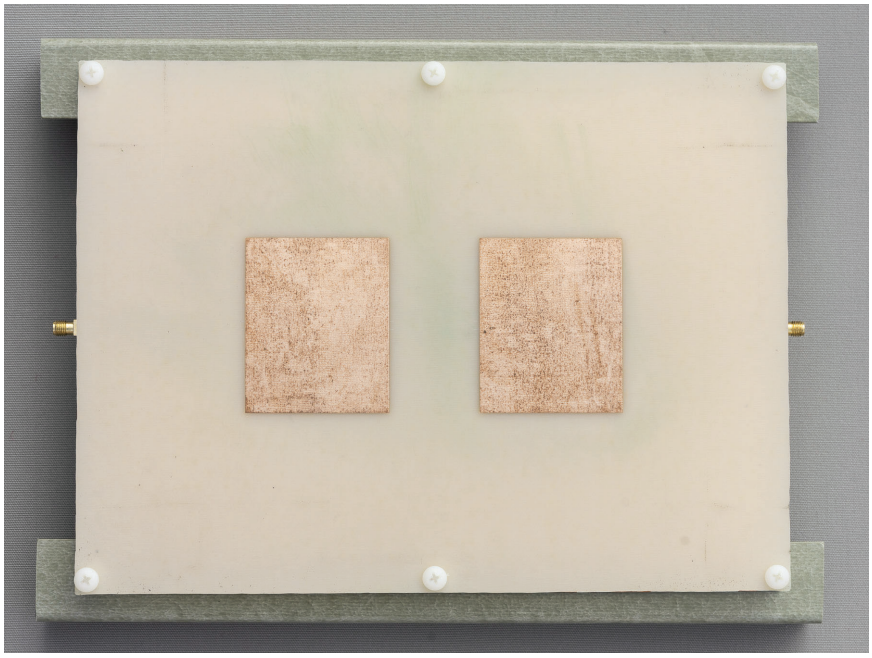

Figure B.2: Assembled 2×1 element uniform rectangular array.

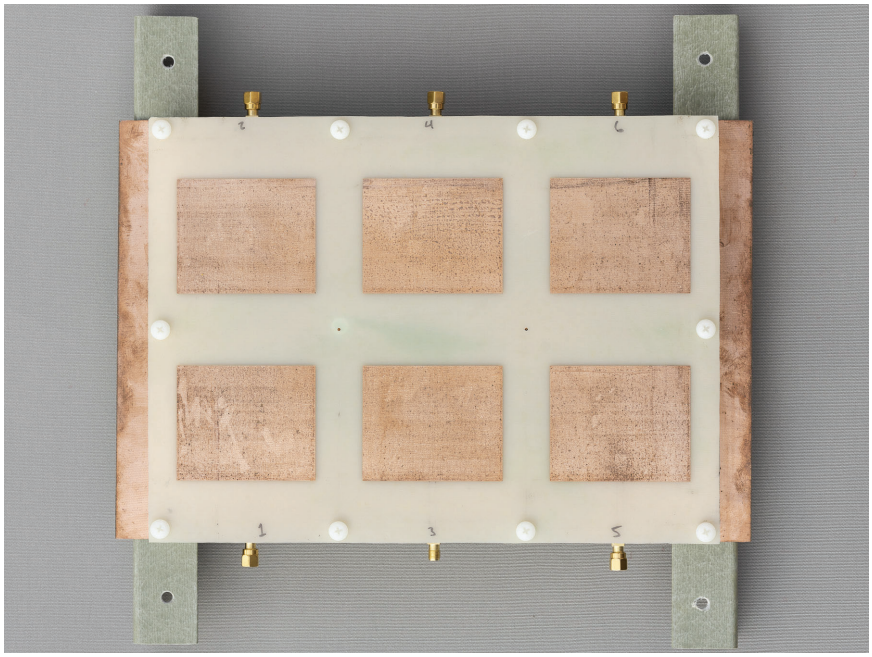

Figure B.3: Assembled 2×3 element uniform rectangular array. SMA port caps are 50Ω terminators.

B.2 Edge-launch SMA to microstrip transition

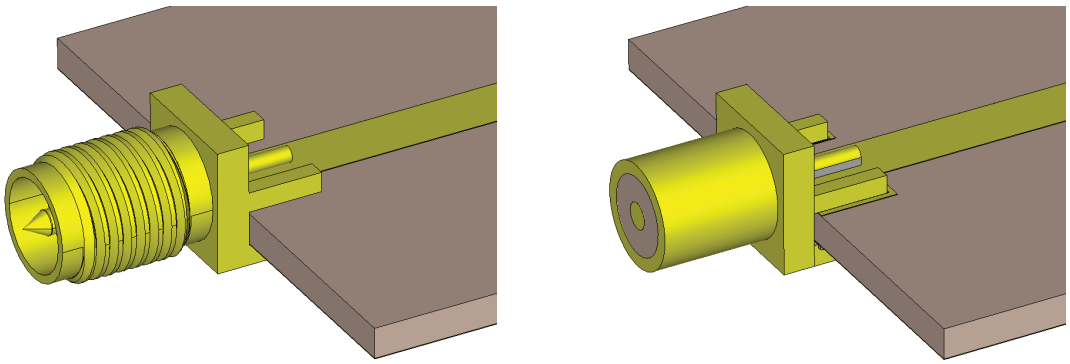

(a) Manufacturer-provided component model.

(b) Simplified model with solder joints used for launch optimization.

Figure B.4: Models of the edge-launch SMA connector. Coaxial dielectric is PTFE ($\varepsilon_r = 2.1$).

An interface is required to connect the microstrip transmission lines used for the array feeds to the test instrumentation, generally coaxial transmission lines with SMA connectors. Microstrip to SMA transitions were designed to integrate edge-launch connectors from RF Solutions (p/n CON-SMA-EDGE-S).[2] Edge-launch connectors were preferred for the subarray prototypes, since they can transition directly to a microstrip transmission line, do not require any through-holes, and every element in the subarray has an adjacent PCB edge.

Numerical models were used to optimize the SMA to microstrip launch geometry, as used on all test articles in this work, with a time-domain solver. Dimensional discrepancies and geometry errors in the manufacturer-provided connector model seen in Figure B.4a prevented its use in numerical simulations. A simplified model was created to capture the essential features while including the solder joint and a small air gap between the connector and PCB, enforced by a step in the center pin. This model, illustrated in Figure B.4b, was used to estimate the reflection coefficient and impedance match, with a matched waveguide point on the SMA connector (port 1) and on the far end of the microstrip transmission line (port 2).

Using the simplified connector geometry obtained from the manufacturer-provided dimensions and measurements of individual connectors, the line impedance at port 1 was estimated at 45Ω. A simulated time-domain reflectometry experiment, illustrated in Figure B.5, shows this impedance mismatch between the connector and the 50Ω microstrip transmission line; the spatial resolution is limited by the maximum frequency component (50 GHz), determined by computational limits on mesh size. Additional mismatch at the coaxial to microstrip interface is not fully resolved.

[2] At $1.70 per connector from US suppliers, this component represented the bottom end of the commercial connector market, but is specified for adequate performance up to 6 GHz.

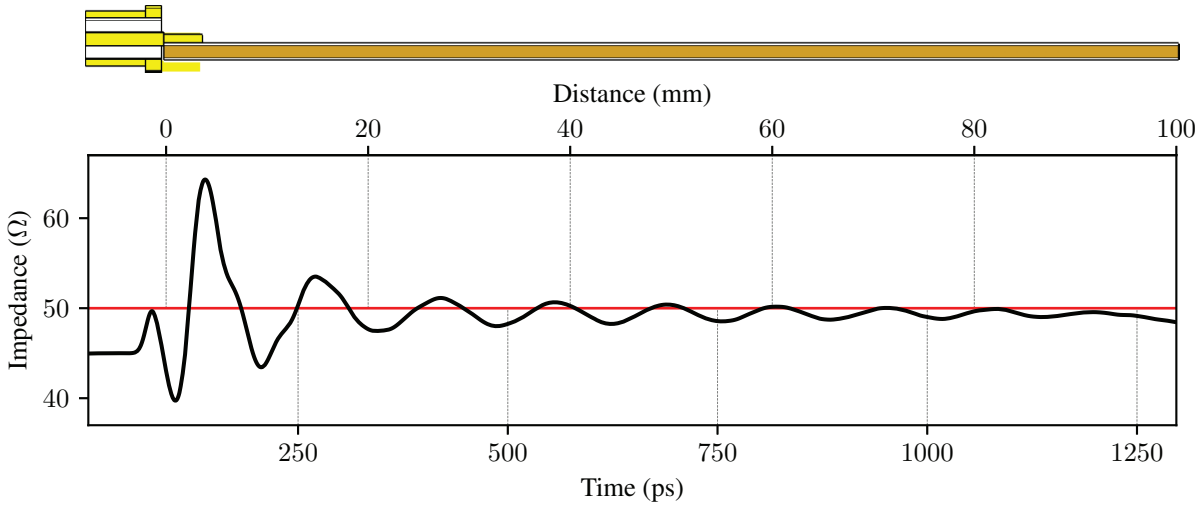

Figure B.5: Simulated time-domain reflectometry of the edge launched SMA to FR4 microstrip transition. Distance scale based on a constant velocity factor $1/\sqrt{\varepsilon_{eff}}$ where $\varepsilon_{eff} = 3.26$ is the effective dielectric constant for the microstrip transmission line. Microstrip transition uses geometry (b) from Figure B.6. Model excitation source is a Gaussian pulse with 17.52 ps rise time.

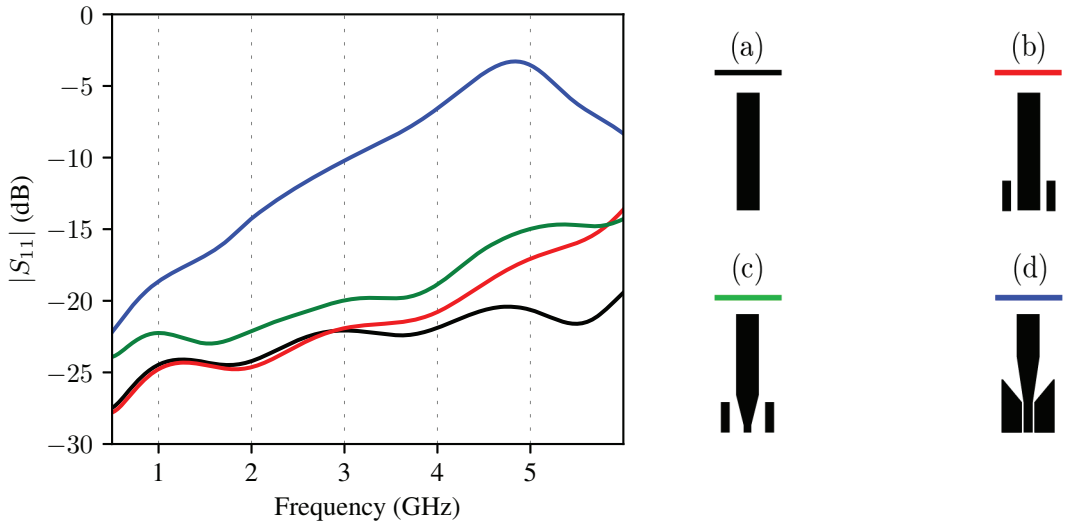

Figure B.6: Simulated reflection coefficient magnitude for the simplified SMA edge connector model in Figure B.4b combined with different copper pours transitioning to 50Ω microstrip transmission line: (a) straight microstrip, upper ground pins on SMA connector filed off to reduce stray capacitance; (b) straight microstrip with minimum-area pads; (c) microstrip tapered to counteract stray capacitance; (d) pseudo-coplanar waveguide to microstrip transition. Geometry (b) was used in all manufactured test articles.

The reflection coefficient magnitude $|S_{11}|$ was estimated for four launch geometries, illustrated in Figure B.6. Geometry (a) minimizes stray capacitance at the transition by additionally deleting the upper pair of ground legs on the connector body. This compromises the mechanical strength of the connector; geometry (b) provides minimum-area pads for mechanical attachment, and the simulated reflection coefficient is approximately identical below 3 GHz. Geometry (c) and (d) attempt to compensate for the stray capacitance with an additional inductance, or by transitioning to the microstrip transmission line from a pseudo-coplanar waveguide, but neither design offered improvement over the straight microstrip. Geometry (b) was used on all fabricated subarray ports.

B.3 Ring resonator

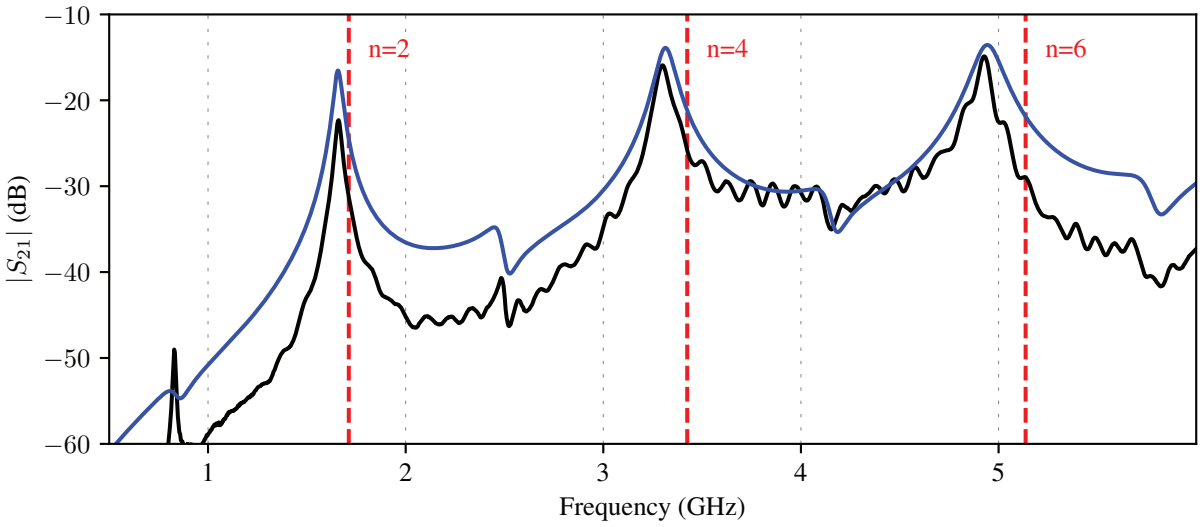

Figure B.7: Two-port ring resonator measurement — compared to a simple transmission line model without feed coupling - - - and an explicit numerical model —. Both models use $\varepsilon_r = 4.3$.

The low-cost FR4 substrate used in this work was not manufactured with a controlled dielectric constant. A two-port microstrip ring resonator with capacitively-coupled microstrip feeds separated by $90°$ was constructed to verify the value of the dielectric constant used for numerical optimization, before fabricating the antenna subarrays.

The ring resonator is a good approximation of a straight microstrip, provided that the ring radius is large compared to the microstrip width. Following a simple transmission line model, the two-port network is resonant at wavelengths corresponding to even multiples of its mean circumference, $\lambda = {}^{2\pi r}/_{n}$ where n is an even integer. Compared to a linear microstrip resonator, the ring topology avoids end effects from fringing fields and ground plane boundaries, averages out anisotropy in the measured dielectric constant arising from the biaxial glass weave in the substrate, and has only a small number of dimensional variables that influence the measured value of ε_r [55].

As constructed, the resonator consisted of a 50Ω microstrip ring with a mean diameter of 62 mm and 50Ω microstrip feeds capacitively coupled with a 0.2 mm gap. The nominal $n = 2$ harmonic frequency for this geometry is 1712 MHz. Edge-launch SMA connectors provided test ports. Several stages of the fabrication process are illustrated in Figure B.8.

Predictions from a transmission line model and an explicit numerical model using $\varepsilon_r = 4.3$ are compared with measurements from an HP 8753D VNA in Figure B.7. The 0.2 mm coupling gap is very small relative to the microstrip width and the measured resonant frequency is lower than predicted by a transmission line model for an isolated ring decoupled from the feed network; this feedline coupling can be incorporated in an analytical transmission line model [56] but validation against the explicit numerical simulation is sufficient for subsequent array models. The value $\varepsilon_r = 4.3$ is used for the FR4 dielectric constant throughout this work.

(a) Design printed on transfer paper.

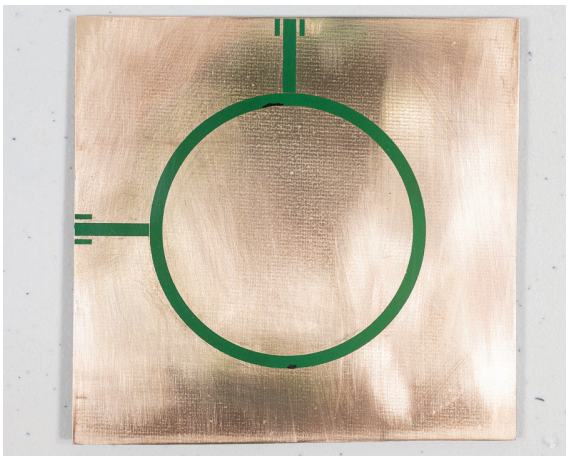

(b) Design on copper after toner pattern transfer and sealing.

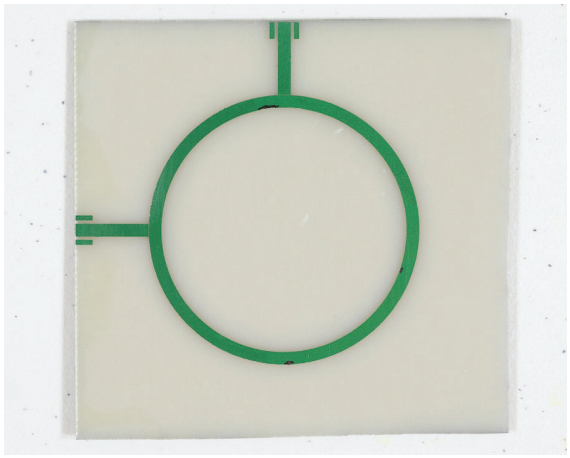

(c) Design after etching.

(d) Finished product after cleaning. SMA edge-launch connectors not installed.

Figure B.8: Fabrication of a two-port microstrip ring resonator used to measure the dielectric constant of the FR4 substrate.